Journal of Medicinal Chemistry

Article

The Discovery and Development of a Series of Pyrazolo[3,4-*d*]pyridazinone Compounds as Novel Covalent Fibroblast Growth Factor Receptor (FGFR) Inhibitors by Rational Drug Design

Yulan Wang, Yang Dai, Xiaowei Wu, Fei Li, Bo Liu, Chunpu Li, Qiufeng Liu, Yuanyang Zhou, Bao Wang, Mingrui Zhu, Rongrong Cui, Xiaoqin Tan, Zhaoping Xiong, Jia Liu, Minjia Tan, Yechun Xu, Mei-Yu Geng, Hualiang Jiang, Hong Liu, Jing Ai, and Mingyue Zheng

J. Med. Chem., **Just Accepted Manuscript** • DOI: 10.1021/acs.jmedchem.9b00510 • Publication Date (Web): 23 Jul 2019

Just Accepted

is published by the American Chemical Society. 1155 Sixteenth Street N.W., Washington, DC 20036

of Sciences, State Key Laboratory of Drug Research; ShanghaiTech University
Liu, Hong; Shanghai Institute of Materia Medica Chinese Academy of Sciences, Key Laboratory of Receptor Research
Ai, Jing; Shanghai Institute of Materia Medica Chinese Academy of Sciences, State Key Laboratory of Drug Research; University of the Chinese Academy of Sciences
Zheng, Mingyue; Shanghai Institute of Materia Medica Chinese Academy of Sciences, State Key Laboratory of Drug Research

The Discovery and Development of a Series of Pyrazolo[3,4-*d*]pyridazinone Compounds as Novel Covalent Fibroblast Growth Factor Receptor (FGFR) Inhibitors by Rational Drug Design

Yulan Wang[1, †], Yang Dai[1, †], Xiaowei Wu[2, †], Fei Li[1, 3], Bo Liu[1], Chunpu Li [1, 2], Qiufeng Liu[2], Yuanyang Zhou[1, 4], Bao Wang[2, 5], Mingrui Zhu[1], Rongrong Cui[1], Xiaoqin Tan[1, 4], Zhaoping Xiong[1, 5], Jia Liu[1], Minjia Tan[1], Yechun Xu[2], Meiyu Geng[1], Hualiang Jiang[1, 5], Hong Liu[2, *], Jing Ai[1, 4, *], Mingyue Zheng [1, *]

[1] State Key Laboratory of Drug Research, Shanghai Institute of Materia Medica, Chinese Academy of Sciences, 555 Zuchongzhi Road, Shanghai 201203, China
[2] Key Laboratory of Receptor Research, Shanghai Institute of Materia Medica, Chinese Academy of Sciences, 555 Zu Chong Zhi Road, Shanghai, 201203, China
[3] School of Chemistry, ShangHai University, 99 ShangDa Road, ShangHai 200444, China
[4] University of Chinese Academy of Sciences, No.19A Yuquan Road, Beijing 100049, China
[5] School of Life Science and Technology, ShanghaiTech University, 393 Middle Huaxia Road, Shanghai 200031, China

ABSTRACT

Alterations of fibroblast growth factor receptors (FGFRs) play key roles in numerous cancer progression and development, which makes FGFRs attractive targets in cancer therapy. In the present study, based on a newly devised FGFR target-specific scoring function, a novel FGFR inhibitor hit was identified through virtual screening. Hit-to-lead optimization was then performed by integrating molecular docking and site-of-metabolism predictions with an array of *in vitro* evaluations and X-ray cocrystal structure determination, leading to a covalent FGFR inhibitor **15**, which showed a highly selective and potent FGFR inhibition profile. Pharmacokinetic assessment, protein kinase profiling and hERG inhibition evaluation were also conducted, and they confirmed the value of **15** as a lead for further investigation. Overall, this study exemplifies the importance of the integrative use of computational methods and experimental techniques in drug discovery.

INTRODUCTION

The fibroblast growth factor receptor (FGFR) family is a subfamily of receptor tyrosine kinases (RTKs), which comprises four highly conserved transmembrane receptor tyrosine kinases, FGFR1, FGFR2, FGFR3 and FGFR4.[1] FGFRs play important roles in a variety of cell functions, such as cell proliferation and differentiation, and biological processes, including development, angiogenesis, homeostasis, and wound repair.[2] Alterations of FGFRs are associated with the progression and development of several cancers, and they contribute to carcinogenesis in three main situations, namely, driver mutations, neoangiogenesis and resistance to anticancer agents. Extensive FGFR alterations in cancers have been observed, such as FGFR1 amplifications in 6% of small cell lung carcinomas, 20% of squamous non–small cell lung carcinomas,17% of osteosarcomas, 10%~15% of breast cancers, 5% of ovarian cancers and 9% of esophageal cancers; FGFR2 translocations in 14% of intrahepatic cholangiocarcinomas; FGFR2 mutations in 12%~14% of endometrial cancers and 5% of squamous non-small cell lung carcinomas; FGFR2 amplifications in 12%~14% of gastric cancers and 4% of breast cancers; FGFR3 translocations in 3%~6% of bladder carcinomas, 3% of glioblastomas and 15%~20% of myelomas; FGFR3 mutations in 60%~80% of non-muscle-invasive bladder carcinomas; FGFR4 mutations in 6%~8% of rhabdomyosarcomas; etc.[3] Therefore, targeting FGFRs with small-molecule inhibitors represents a promising therapeutic strategy for treating the above FGFR-related cancers.[4]

A large amount of effort has been devoted to developing FGF/FGFR inhibitors as anticancer treatments.[5] Several classes of small-molecule FGFR inhibitors have been reported, and they can be clustered into two classes based on their inhibition profiles. The first class of inhibitors are characterized by “multitarget” tyrosine kinase inhibitors (TKIs), which have broad targets, including FGFR. In addition to FGFR, these “multitarget” TKIs may also target vascular endothelial growth receptors (VEGFRs), platelet-derived growth factor receptors (PDGFRs) and other tyrosine kinases, resulting in serious adverse effects in clinical studies, in particularly VEGFR2-based dose-limiting toxicities.[6-8] The second class is inhibitors with highly selective and potent inhibitory activities against FGFR. These compounds can specifically target FGFR, reducing the risks of side effects in clinical usage and making the mechanism of action (MOA) easier to study. According to their MOA, FGFR-selective inhibitors fall into two categories: noncovalent inhibitors and covalent inhibitors. To date, several selective inhibitors, including both

noncovalent and covalent inhibitors (shown in **Figure 1**; noncovalent inhibitors: AZD4547[9] (**1**), NVP-BGJ398[10] (**2**), E7090[11] (**3**), LY2874455[12] (**4**), JNJ-42756493[13] (**5**), and CH5183284[14] (**6**); covalent inhibitors: TAS 120[15, 16] (**7**)) are in clinical development, and some have demonstrated clinically meaningful benefits with manageable toxicity profiles in clinical trials. For example, **1**, a selective reversible FGFR inhibitor, has demonstrated a well-tolerable safety profile and modest antitumor activity in advanced squamous cell lung cancers in a phase Ib study.[17] In a phase Ib/IIa study, a combination of **1** with either anastrozole or letrozole showed anti-tumor activity in advanced estrogen receptor-positive breast cancers resistant to aromatase inhibitors.[18] In addition, a selective covalent FGFR inhibitor, **7**, has shown a tolerable safety profile and antitumor activity in patients with cholangiocarcinoma harboring FGFR2 gene fusions and cholangiocarcinoma (CCA) patients with FGFR2 gene fusion resistance prior to the FGFR inhibitor **2**.[15, 16, 19] A phase II study of **7** with patients with intrahepatic CCA harboring FGFR2 gene fusions has been initiated. Despite the advances made in FGFR inhibitors, the road to clinical treatment of various diseases related to alterations of FGFR remains long and challenging. The structural diversification of highly selective and highly bioactive FGFR inhibitors is still in high demand, and the options for the clinical treatment of diverse FGFR aberrations in a wide variety of cancers are still very limited, highlighting the importance of developing FGFR inhibitors of novel chemotypes.

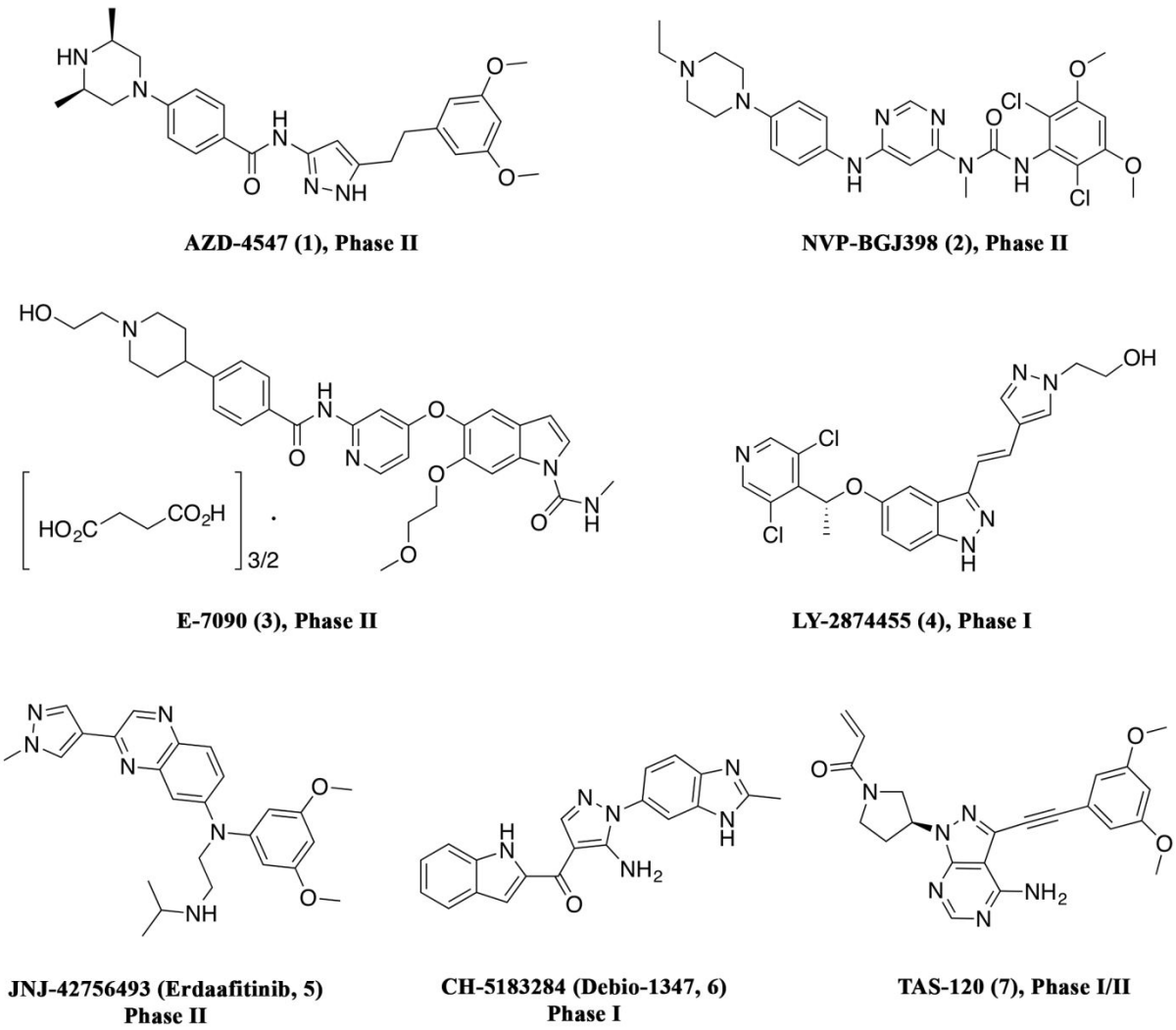

Figure 1. FGFR-selective inhibitors in clinical development.

The current study reports the discovery and development of a series of pyrazolo[3,4-*d*]pyridazinone derivatives as a novel type of FGFR inhibitors, and it emphasizes the synergetic use of computer-aided drug design (CADD) with experimental evaluations to address different issues in our hit identification and hit-to-lead optimization stages. Moreover, a variety of chemical, biophysical and bio-pharmacological methodologies were used for the full characterization of the anticancer activity, physicochemical and PK properties, and mechanism of action (MOA) of the discovered FGFR inhibitor **15**, which may serve as a promising new lead for developing potential anticancer treatments.

RESULTS AND DISCUSSION

1. Hit Discovery by Target Specific Scoring Function and Virtual Screening

The target-specific scoring function has proven effective in enhancing the enrichment of virtual screening (VS) for novel hit discovery, and for interpreting the subtle commonalities and differences in the ligands binding to the target binding site of interest. Previously, we built a target-specific scoring function for methyltransferases, SAMscore, based on the crystal structures of methyltransferase and their ligands activity.[20] The SAMscore demonstrated improved scoring ability and has been successfully used to identify novel disruptor of silencing telomeric 1-like inhibitors.[20] To date, the crystal structures of many FGFR proteins and FGFR inhibitors have been reported, providing the basis for the development of FGFR target-specific scoring functions. In this study, using a workflow similar to that of SAMscore, we developed a target-specific scoring function for FGFR, RTKscore. First, we selected protein crystal structures for FGFR1, FGFR2 and FGFR3, and the PDB codes were 3TT0[10], 2PVF[21] and 4K33[22], respectively. In addition, 1,090 FGFR ligands with known chemical structural information and activity data were collected from Binding DB.[23] The ligands with reported inhibitory activity data such as > 10^9 nM were marked as inactive. Second, the molecular docking program Glide[24] was used to generate the binding modes of the FGFR proteins and their ligands. The iterative potential of mean force (iPMF)[25] features of the binding mode of each ligand with the corresponding protein were calculated to characterize the interaction between the ligand and the protein as the input data for modeling building the model. Third, original features were processed and selected with the machine learning methods epsilon support vector regression (ε-SVR)[26] and RFE[27], in which the features were removed stepwise according to their importance to the model. Here, the importance of each feature was evaluated by calculating the square of its Pearson correlation coefficient (R^2) with the ligands' affinity data. Similar to our previous report,[20] iPMF features were calculated to characterize the protein-ligand interactions, and these features included the pairwise interaction features involving 17 types of atoms in the protein, 30 types of atoms in the ligands, and 11 distance ranges. In this study, a total of 1,125 features were selected for further model building. A five-fold cross validation process was used to evaluate performance of the model. Finally, we obtained a model called RTKscore with reasonable prediction ability; the R^2 of its 5-fold cross validation was 0.46. In addition, we compared RTKscore with Glide on a same test set, and RTKscore exhibited a more

significant correlation with the pIC50 values of these ligands (**Figure 2**). The R^2 of RTKscore was 0.59, whereas the R^2 of Glide was near zero.

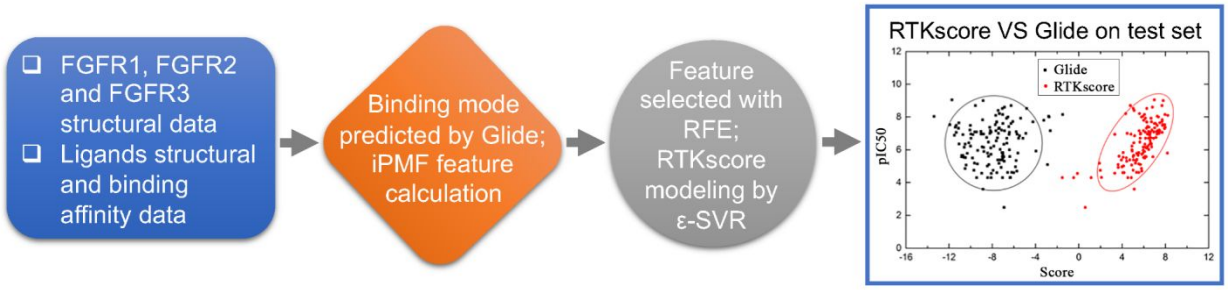

Figure 2. Workflow of RTKscore development and comparation of RTKscore with Glide on a test set.

As described above, the RTKscore showed better predictive performance for FGFR ligands than a general-purpose scoring function. We therefore applied the RTKscore in a VS project for discovering novel FGFR1 inhibitors. The SPECS small-molecule database was used as the ligand databases, and compounds containing any PAINS substructures,[28] inorganic atoms, unwanted functionalities, and reactive groups were filtered out first. There were 190,038 ligands that remained and were prepared for the virtual screening, and Glide was used to generate the potential binding modes of each ligand. The RTKscore was used to rescore the poses of each ligand, which included calculating the iPMF features for each pose, the feature subset extraction and rescoring with the RTKscore. According to the highest score of each ligand, as scored by RTKscore, we kept the top 1,000 ligands for further evaluation. To ensure structural diversity among the ligands for biochemical testing, we clustered ligands into 100 clusters on the basis of their chemical similarities as measured by molecular fingerprints ECFP4,[29] and only one or two ligands from each cluster were selected. Finally, 112 ligands were selected and purchased for FGFR1 inhibitory activity evaluation. We used ELISA assay to test the inhibitory activities of the ligands against FGFR1 at 50 μM and found that compound **8** showed high inhibitory activity against FGFR1, with an IC_{50} of 114.5±15.3 nM. Its inhibitory activity against FGFR1-depended KG1 cell proliferation was tested, and the results showed that this compound could inhibit the proliferation of KG1 cell with IC_{50} = 1107.8±264.7 nM.

2. Hit-to-Lead Optimization by Covalent Inhibitor Design

To better investigate the structure-activity relationships, we used molecular docking to simulate the binding mode of **8** with FGFR1. As shown in **Figure 3B**, the putative binding mode of compound **8** follows the typical pattern of most reported FGFR inhibitors. It may also form hydrogen bonds with the hinge area of FGFR1, in which the pyridazine moiety of compound **8** forms three hydrogen bonds with the residues Ala564 and Glu562. The benzofuran moiety of compound **8** was located in the hydrophobic pocket of the protein active site, and the N-phenyl substituent of the ligand reached the solvent-exposed area of the loop part of the protein. Based on the putative binding mode of **8** with the FGFR1 protein, we found that the hydrophobic pocket of FGFR1 has additional space (**Figure 3C**). To better accommodate the hydrophobic pocket, we first explored benzofuran substituents. After testing a few kinds of substituents, we found that compound **9** with a 3,5-dimethyl-2-benzofuran moiety shows more potent inhibitory activities, with FGFR1 IC_{50} = 10.8±1.3 nM and KG1 cell IC_{50} = 415.7±8.7 nM.

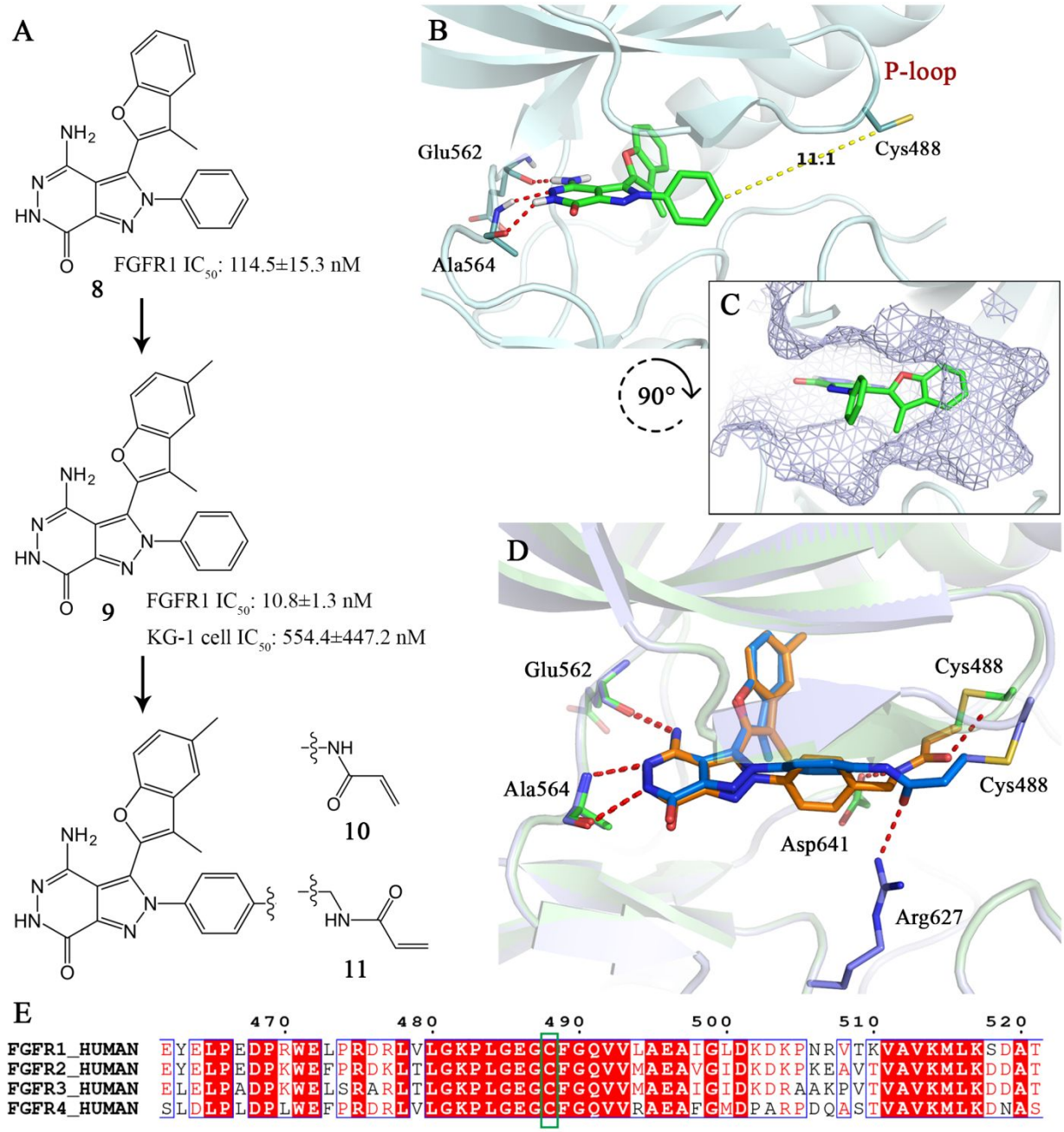

Figure 3. (A) The structures of compounds **8**, **9**, **10** and **11**; (B) putative binding mode of compound **8** with FGFR1(PDB code: 3TT0); (C) the active site pocket of FGFR1 depicted as mesh surface. (D) the putative binding modes of compound **10** (blue) and compound **11** (orange) with FGFR1 (PDB code: 3TT0) simulated by covalent docking. (E) FGFR1, FGFR2, FGFR3 and FGFR4 P-loop sequence alignment.

Recently, with the resurgence of covalent inhibitors, more and more covalent small molecule kinase inhibitors have been approved by FDA.[30-32] A large number of kinase targets have a cysteine located in the vicinity of the ATP pocket that could be targeted by irreversible

inhibitors.[33, 34] As for FGFR, covalent targeting the Cys residue in the P-loop of FGFRs is also an effective strategy for developing selective inhibitors.[35] As reported by the Gray laboratory, the covalent inhibitor showed gratifying inhibitory activity against FGFR1 at both the molecular level and cellular level.[35] In this study, the simulated binding mode of **8** implied that its N-phenyl substituent extends out the P-loop of FGFR1, which contains a conserved Cys residue within FGFR family (shown in **Figure 3E** marked with a green box, i.e., Cys 488 in FGFR1). The distance from the phenyl ring of **8** to this Cys residue was 11.1 Å, within the appropriate distance range for a reactive Michael acceptor (**Figure 3B**). Based on this observation, two covalent inhibitors **10** and **11** were designed by introducing Michael acceptor substituents with different distance to the benzene ring of compound **9**. We used covalent molecular docking to simulate the binding mode of **10** and **11** with FGFR1, and the simulated results showed that both compounds could form a covalent interaction with Cys488 of the FGFR1 P-loop without a significant change in their overall binding mode (**Figure 3D**).

3. *In vitro* Activities of Compounds 10 and 11

Compounds **10** and **11** were synthesized and tested for their inhibitory activity against FGFRs and a diverse panel of representative human kinases. As shown in **Table 1**, both **10** and **11** exhibited great inhibitory activity to FGFR1, FGFR2, and FGFR3 *in vitro* (**Table 1**). Meanwhile compound **10** also showed potent inhibitory activity against FGFR4 (**Table 1**). Compounds **10** and **11** showed excellent selectivity for FGFR were observed across typical angiogenesis-regulating kinases, including VEGFR1 and VEGFR2, PDGFRα, PDGFRβ, VEGFR1 and VEGFR2, and other tested human kinases.

Increased FGFR signaling promotes cancer cell proliferation. To elucidate the impact of **10** and **11** on FGFR-mediated cancer cell proliferation, five FGFR-driven cell lines harboring frequently occurring oncogenic forms of FGFRs were chosen: FGFR1-translocated KG1 cells, FGFR2-amplified H716 cells, FGFR2-amplified SNU16 cells, FGFR3-mutant UMUC14 cells, and BaF3/FGFR1 cells. As shown in **Table 1**, compound **10** strongly inhibited cell proliferation of KG1, H716, SNU16, UMUC14 and BaF3/TEL-FGFR1, and most of its IC_{50} values were less than 10 nM, making it more potent than AZD4547. The model cell line BaF3/TEL-VEGFR2, which stably expressed the constitutively active form of TEL-VEGFR2, was used to further assess

the cellular selectivity of compound **10** for FGFR against VEGFR2. As shown in **Table 1**, compared with its high potency against cell proliferation of BaF3/TEL-FGFR1 (IC_{50} < 0.3 nM), compound **10** had no significant inhibitory effect on VEGFR2-mediated cell proliferation (IC_{50} = 6119.8±1040.6 nM), confirming the high selectivity of compound **10** for FGFRs against VEGFR2 at the cellular level.

Table 1. Molecular and cellular inhibitory activity evaluation of compounds **10** and **11**.

Kinase	IC_{50} (nM)			Cell	IC_{50} (nM)		
	10	**11**	**1**		**10**	**11**	**1**
FGFR1	4.8 ± 1.6	16.3 ± 1.1	0.6 ± 0.1	KG1	<0.3	0.6±0.0	3.7±0.6
FGFR2	2.3 ± 0.1	6.6 ± 1.6	0.4 ± 0.0	SNU16	<0.3	1.3±0.1	4.9±0.6
FGFR3	15.0 ± 1.1	12.5 ± 1.2	3.4 ± 0.4	UMUC14	6.4±2.1	36.4±5.3	10.3±0.6
FGFR4	23.1 ± 3.6	>200	49.8 ± 7.6	BaF3/TEL-FGFR1	<0.3	9.8±2.8	0.5±0.0
VEGFR2	>1000	>1000	57.9 ± 22.1	BaF3/TEL-VEGFR2	6119.8±1040.6	>10000	416.9±10.0
VEGFR-1	>1000	67.6%@1000	\				
PDGFR-β	>1000	58.8%@1000	\				
Ret	78.4%@1000	>1000	\				
c-Src	>1000	>1000	\				
c-Met	>1000	>1000	\				
ALK	>1000	>1000	\				
EGFR	>1000	>1000	\				
ErbB2	>1000	>1000	\				
ErbB4	>1000	>1000	\				
EPH-A2	>1000	>1000	\				
ABL	>1000	>1000	\				

To further evaluate the cellular activity of compound **10** for targeting FGFR kinase, we analyzed its effects on the phosphorylation of FGFR and its major downstream signaling molecule, Erk. Two representative human cancer cell lines with FGFR aberrations were used, namely, KG1 and SNU16. We found that **10** showed significant inhibition of the phosphorylation of FGFR1 and FGFR2 in the individual cancer cell lines. The phosphorylation of Erk was also inhibited (**Figure 4**). Thus, at the cellular level, **10** potently inhibits FGFR signaling.

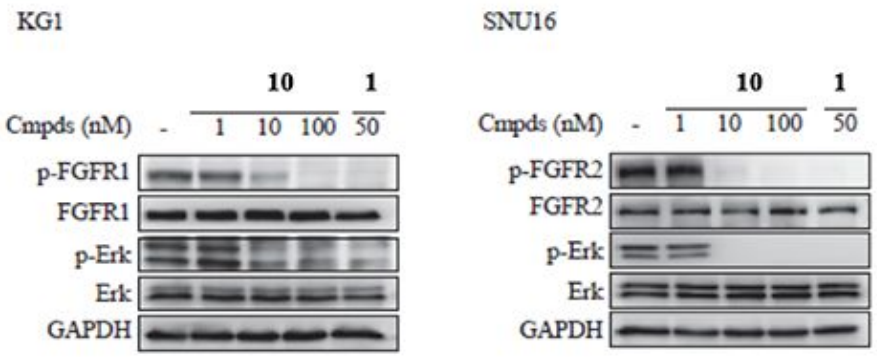

Figure 4. The effects of compound **10** on the phosphorylation of FGFR and the downstream effector Erk in the KG1 and SNU16 cell lines.

4. Investigation of the Covalent Binding Mechanism Investigation

To elucidate the interaction mechanism of this series of compounds, we solved the cocrystal structures of compound **9** in complex with FGFR1 (PDB id: 6ITJ), compound **10** with FGFR4 (PDB id: 6IUP), and compound **11** with FGFR4 (PDB id: 6IUO). Overall, these cocrystal structures provided a solid structural basis for understanding the binding mode of this series of compounds, and also confirmed our molecular design concepts. **Figure 5A** shows the crystal structure overlaid with the predicted structure, where the binding mode of **9** determined in the crystal structure is highly consistent with the binding mode simulated by molecular docking. **Figure 5B** compares the crystal structures of complexed **10** and **11**, which differ from each other by only a -CH_2- group in the acrylamide moiety. As expected, compounds **10** and **11** have binding modes highly similar to that of compound **9**, and the acrylamide moiety of these two compounds reached the targeted Cys residue in the P-loop. The P-loop is highly flexible, and the minor structural differences between the compounds significantly influenced the spatial arrangement of the loop. For compound **11**, a covalent bond with the Cys477 residue of FGFR4 can be observed. For compound **10**, the distance from the carbon atom of the Michael acceptor to the sulfur atom of Cys477 is 2.6 Å, which is slightly longer than the C-S bond length. Because the crystallographic structure is static and represents the spatial average over the whole crystal, we cannot rule out a potential covalent bonding interaction between **10** and FGFR4 given such a short C-S distance and the highly flexibility of the binding site.

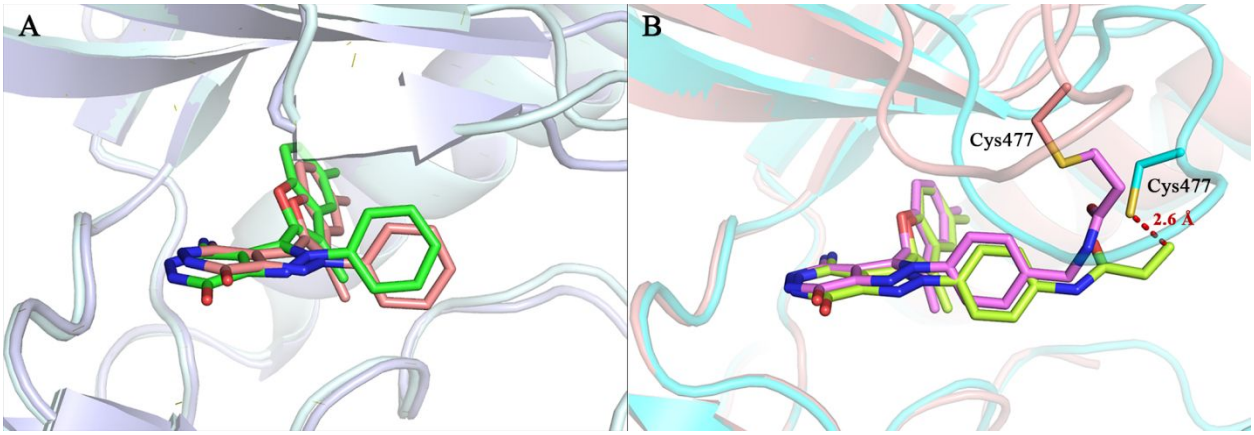

Figure 5. (**A**) The cocrystal structure (shown in green) of compound **9** and the FGFR1 complex (PDB id: 6ITJ) and the putative binding mode (shown in pink) of compound **9** and FGFR1 simulated by molecular docking. (**B**) The crystal structures of the complex of compound **10** (shown in magenta) with FGFR4 (shown in salmon) (PDB id: 6IUP) and the complex of compound **11** (shown in lemon) with FGFR4 (shown in cyan) (PDB id: 6IUO).

To investigate the potential covalent bond between **10** and FGFR4, we used protein mass spectrometry to analyze the amino acid residues modified by compound **10** in the FGFR4 kinase domain. The FGFR4 kinase domain protein was incubated with compound **10** and digested with trypsin. Then, the tryptic peptides were subjected to LC-MS/MS analysis. The MASCOT program was used to identify protein modification by searching the Uniport database. The target peptide, LVLGKPLGEGCFGQVVR (the peptide contains the Cys residue that may be covalently bound), has been identified (**Figure S1**). Further analysis showed that the Cys residue of the peptide, LVLGKPLGEGCFGQVVR, was modified by 440.46 Da, which exactly matches the molecular weight of a compound **10** (**Figure S2**). These results indicated that compound **10** could bind to the FGFR4 protein and form specifically a covalent bond with the residue of Cys477.

5. Optimization of PK Properties

The pharmacokinetics (PK) properties of compound **10** in rat were determined, and it showed low oral bioavailability in rats (**Table 4**). To improve the PK profile of **10**, we first used site-of-metabolism (SOM) prediction programs to identify the reactive sites of **10**. Three SOM prediction programs were used: SOME-UGT[36, 37], SMARTCyp[38] and the metabolism prediction module[39] of Maestro (Schrödinger LLC, New York, NY, 2015). The 5-methyl group on the benzofuran moiety was predicted to be a reactive site by all three programs (**Figure 6**). In addition, the Michael acceptor moiety that is prone to nucleophilic reactions. Overall, we considered that

the Michael acceptor of **10** and the 5-methyl group on the benzofuran are high priorities for site modification.

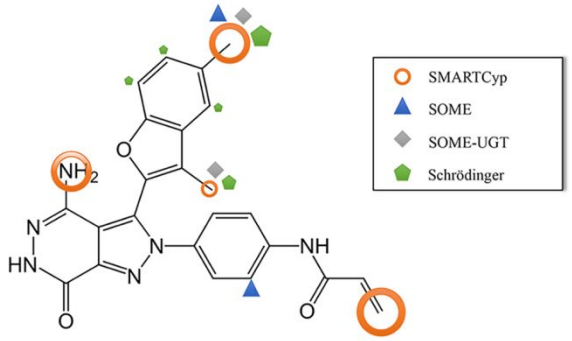

Figure 6. SOM prediction of compound **10** by three programs. SMARTCyp (orange circles, metabolism probability ordered by size of circle), SOME (blue triangles) and SOME-UGT (grey diamonds), and Schrödinger (green pentagons, metabolism probability ordered by size).

The optimization of the covalent reactive groups is a key challenge in covalent drug design. An ideal reactive group should have sufficient reaction activity to form the desired bond with the target protein, but indiscriminate and high reactivity may lead to insurmountable PK problems and toxicity in the late stage of drug development.[40, 41] For compound **10**, we aim to slightly weaken the reactivity of the Michael acceptor, to reduce its binding to off-target nucleophiles, for example, glutathione (GSH) and proteins with exposed nucleophilic centers such as serum albumin. These unspecific interactions may account for the fast clearance of **10**. Several studies have reported that a useful optimization strategy is to add an *N,N*-dimethylaminomethyl substituent or an analogues to the end of the Michael acceptor,[42, 43] which would not only reduce the electrophilicity but also enhance the steric hindrance of the Michael acceptor. Moreover, a basic functional group onto the Michael acceptor of the ligand would improve the reactivity between the ligand and the target protein by catalyzing the intramolecular Michael addition and/or having an inductive effect from the protonated basic group.[44] Thus, we substituted the Michael acceptor moiety of compound **10** with several different amino methyl substituents.

Regarding the 5-methyl group on the benzofuran moiety of **10**, the methyl group can be replaced with a halogen to improve metabolic stability in a straight forward manner. In this study, we replaced the 5-methyl group with two different halogen atoms: chlorine and bromine. As shown in **Table 2**, five derivatives were synthesized for biochemical and metabolic evaluation. First, we tested the inhibitory activities of these derivatives against FGFR1 and FGFR2, and their inhibitory

activities on the proliferation of KG1 cells and SUN16 cells. The results suggested that these structural modifications retained the *in vitro* activities of these compounds. All of these derivatives potently inhibit FGFR1 and FGFR2 enzymatic activity and effectively inhibit the proliferation of FGFR1-depended cancer cells KG1. Second, we compared the solubility of these compounds using a kinetic solubility determination assay. Among them, compounds **10** and **12** showed poor solubility (20 μM), and compounds **13**, **14** and **16** were more soluble, with solubilities comparable to that of ibrutinib[45] (**17**) (an anticancer drug with low solubility[46]), and compound **15** showed the highest solubility (200 μM, **Table 2**). The metabolic stability of compounds **10**, **12**, **13** and **15** in mouse liver microsomes were evaluated. As shown in **Table 2**, *in vitro* $T_{1/2}$ values for the four compounds ranged from 29 min for compound **12** and 31 min and 63 min for compound **10** and compound **13**, respectively, up to 103 min for compound **15** which showed the best stability in mouse liver microsomes because of the longest half-life.

Table 2. Derivatives of compound **10** and their biochemical and metabolic evaluation.

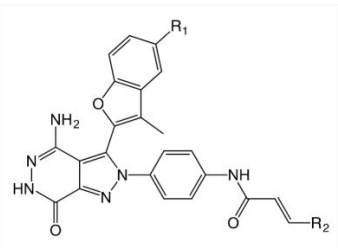

10: $R_1 = CH_3$, $R_2 = H$

12: $R_1 = Cl$, $R_2 = H$

13: $R_1 = CH_3$, $R_2 =$ 

14: $R_1 = CH_3$, $R_2 =$ 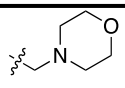

15: $R_1 = Cl$, $R_2 =$ 

16: $R_1 = Br$, $R_2 =$ 

Compound ID	FGFR1 (nM)	FGFR2 (nM)	KG1 cell (nM)	Solubility at pH 7.4 (μM)	Microsomal stability *in vitro* $T_{1/2}$ (min)
10	1.2±0.3	1.5±0.1	<0.3	20	31
12	0.8±0.3	1.1±0.0	<0.3	20	29
13	2.4±0.1	1.9±0.7	<0.3	50	63
14	30.9±7.3	8.0±0.7	2.7±1.4	50	--
15	20.4±0.9	7.2±3.6	3.7±2.5	200	103
16	0.4±0.1	2.0±0.0	0.4±0.1	50	--
1	0.6 ± 0.1	0.4±0.0	8.3 ± 2.1	--	--
17	--	--	--	50	--
18	--	--	--	200	--

To cost-effectively evaluate the reactivity of the designed covalent inhibitors, their undesirable reactions with GSH protein were evaluated *in vitro*. GSH protein was incubated separately with compounds **10**, **13**, **15**, and **16** separately, and then their GSH binding metabolites were determined with LC-MS/MS, and covalent drugs **17** and afatinib[47] (**18)** were chosen as controls. As shown in **Figure 7A**, the GSH adduct of **10** was the only quickly generated metabolite, and other compounds demonstrated comparable stabilities toward off-target thiols of GSH. Thus, we supposed that the poor PK profile of compound **10** is mainly caused by its high intrinsic chemical reactivity profile, and the modified acrylamide functional groups in compounds **13**, **15** and **16** have acceptable reactivity profiles compared with the covalent drugs on the market. This argument is further supported by the following rat whole blood stability assay,[48, 49] in which we incubated compounds **13** and **15** in whole blood for 5 h and detected the remaining parent compounds at different time points. As shown in **Figure 7B**, the prototype of compound **10** decreased quickly, and compound **15** decreased relatively slowly. Moreover, after 5 h, with **10**, the parent compound tended to be depleted, while 20% of compound **15** remained. In general, compound **15** showed good solubility, a weaker binding affinity for GSH, and improved stability in whole blood. Therefore, we chose **15** as the lead compound for further characterization.

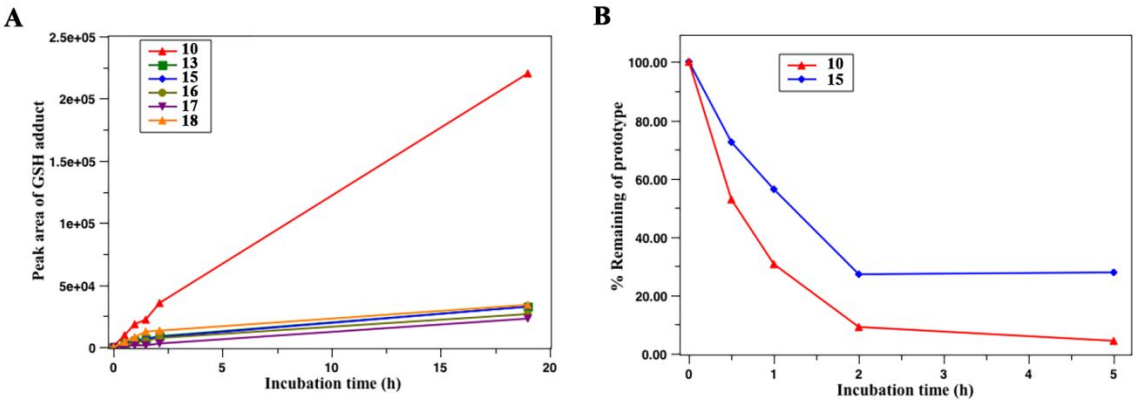

Figure 7. (A) GSH affinity evaluation of compounds **10**, **13**, **15**, and **16**; (B) blood stability evaluation of compounds **10** and **15**.

6. Characterization of Lead Compound 15

Biochemical Kinetic profiling. We further did the kinetic assessment of compounds **10** and **15**. The FGFR1 was used as the representative target kinase. At first, a classic diluting assay was conducted to determine whether compounds **10** and **15** inhibited FGFR via irreversible binding. As shown in **Figure 8**, in contrast to the known reversible FGFR inhibitor **1** that dissociate quickly

allowing recovery of enzyme activity, compounds **10** and **15** markedly prevent recovery of enzyme activity, strongly supporting the irreversible binding mode of compounds **10** and **15** to FGFR1.

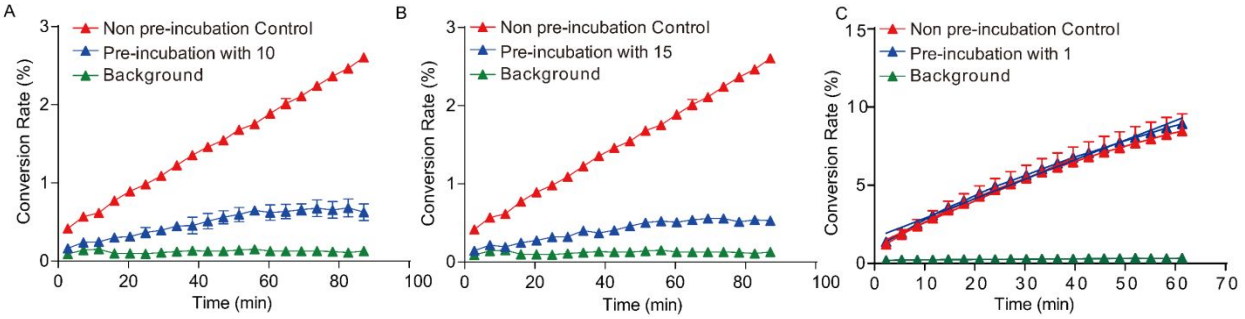

Figure 8. Compound **10** (A) and **15** (B) irreversibly binds to FGFR1. Enzyme activity of FGFR1 was assayed by a Caliper EZ Reader under three different conditions: without the enzyme (background), without the compound (non-pre-incubation control), and pre-incubated with the compound. "Conversion" here represents the enzyme activity and means "the percent of conversion of the substrate peptide".

Then, we conducted traditional kinetics analysis measuring K_{inact}/K_i which defines the second order rate constant for covalent binding to the target protein.[50] The efficient covalent target engagement is apparent for compound **10** and **15** to FGFR1 with a calculated K_{inact}/K_i ratio of 0.38, 0.070 (μM^{-1} s^{-1}), respectively (**Table 3**). This K_{inact}/K_i value was comparable to some EGFR covalent inhibitors or FGFR covalent inhibitor.[51, 52] In addition, compared with compound **10** (K_i = 1.9 nM), weaker affinity for compound **15** to FGFR1 (K_i = 10 nM) was observed, which is consistent with the biochemical and cellular IC_{50} data (**Table 2**). The kinetics studies also suggested covalent irreversible binding of the compound **10** and **15** to FGFR.

Table 3. Kinetics values of compounds **10** and **15** binding to FGFR1.

Compound ID	K_{inact} (s^{-1})	K_i (nM)	K_{inact}/K_i (μM^{-1} s^{-1})
10	7.2×10^{-4}	1.9	0.38
15	7.1×10^{-4}	10	0.070

Protein kinase profiling. To better understand the general kinase target selectivity trends and potential toxicity poisonousness of compound **15**, the commercial KinaseProfiler Service (Eurofins Scientific, Inc.) was utilized to evaluate the selectivity of **15** against a panel of 405 kinases at three fixed concentrations (10 nM, 100 nM and 1000 nM). The KinaseProfiler assay

protocols measure the percent inhibition of phosphorylation of a peptide substrate in the presence of a fixed concentration of ATP (10 μM). Remarkably, compound **15** showed high specificity for FGFR kinases over all other kinases tested, and no appreciable inhibition of the other kinases was observed in the presence of 10 nM, with most maintaining >70% of their control activity. At a concentration of 100 nM, compound **15** inhibited a small number of kinases other than FGFRs, including c-RAF, SIK, DDR1, Arg, Yes, Flt1, and DNA-PK. The location of the profiled kinases and active interactions depicted in a kinase dendrogram tree is shown in **Figure 9**. Details of profiles including all the data from the Eurofins Kinaseprofiler (405 targets) are available in Supporting Information. This experiment further supported that compound **15** has high selectivity for the FGFR family.

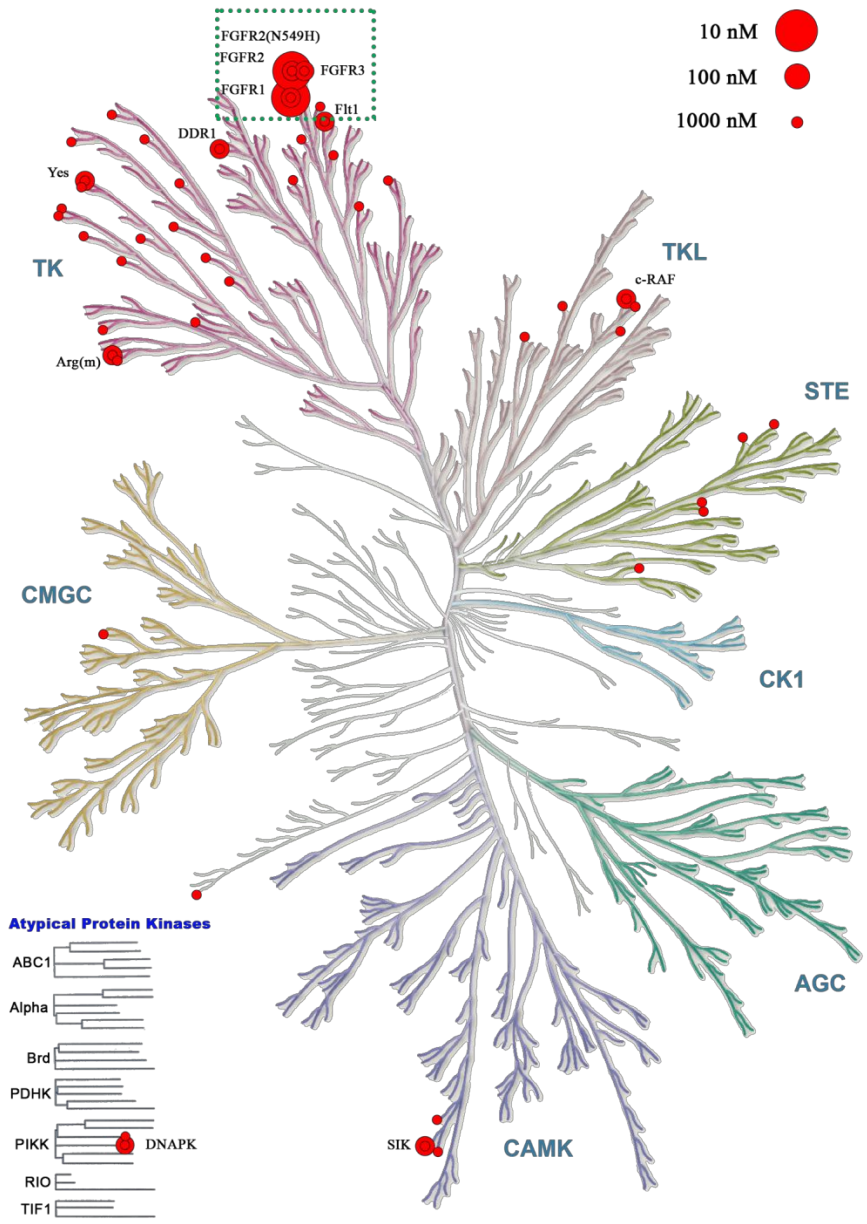

Figure 9. Kinase profile of compound **15** drawn with KinMap.[53] Kinase inhibition ratios above 50% at corresponding concentrations are marked as red circles.

In vivo PK evaluation. The *in vivo* PK evaluation of compound **15** was performed in rats via IV (10 mg/kg), PO (20 mg/kg) and IP (20 mg/kg). Compared with compound **10**, the PK profile of compound **15** shows a significant improvement. As summarized in **Table 4**, when dosing via IV, the plasma exposure of compound **15** was $AUC_{0\text{-}t}$ = 4412.8 ng·h/mL that was four times of compound **10**, and the half-life period of compound **15** was 8.55 h. When dosing via IP, the plasma exposure was $AUC_{0\text{-}t}$ = 16790.8 ng·h/mL and the half-life period was 4.63 h. Unfortunately, when

dosing via PO, the bioavailability of **15** was almost zero. The results revealed that **15** has an acceptable PK profile only when dosing via IV and IP.

Table 4. Pharmacokinetic properties of compounds **10** and **15** in SD rats.

		Dose (mg/kg)	T_{max} (h)	C_{max} (ng/mL)	AUC_{0-t} (ng·h/mL)	$AUC_{0-\infty}$ (ng·h/mL)	MRT (h)	$t_{1/2}$ (h)	CL (L/h/kg)	V_{ss} (L/kg)	F (%)
10	IV	10	0.083	1878.0	1093.9	1272.4	5.04	6.25	8.60	--	--
	PO	20	0.861	12.9	6.4	6.4	2.17	1.77	--	--	0.29
15	IV	10	--	--	4308.7	4412.8	1.64	8.55	2.27	28.0	--
	PO	20	0.5	7.3	32.6	51.5	7.33	21.64	--	--	~0
	IP	20	0.5	5042.5	16790.8	16984.3	3.30	4.63	--	--	--

Species difference study. To understand the metabolic species difference of **15**, we used an *in vitro* model of hepatic subcellular fractions to incubate compounds and analyzed the metabolites with UPLC-UV/Q-TOF MS. The metabolites were ranked in ascending order by their mass-to-charge ratio or their LC retention time when the metabolites had the same mass-to-charge ratio. The results of the metabolism of **15** by hepatic subcellular fractions (**Table S4)** show that **15** was comparatively stable that after 180 min of incubation, and only 20% of the parent compounds was metabolized. The main metabolic pathways of **15** are amino oxidation, GSH binding and amino demethylation. **15** is more likely to bind GSH in human and monkey hepatic subcellular fractions than it is in dog, rat and mouse. The proposed metabolic pathways of **15** in the hepatics subcellular fractions are shown in **Figure S3**. Species differences suggested that there are few variations among hepatic metabolic pathways of **15** in dogs, rats, mice, monkeys and humans. In addition, the metabolism of **15** in human hepatic subcellular fractions is simpler than those of other species.

hERG inhibitory activity. A blockade of the hERG channel may cause drug-induced prolongation of the QT interval, which has become a major concern in drug discovery and development. To evaluate the cardiotoxicities of the candidates, we used a patch-clamp experiment to determine the hERG inhibitory activities of compounds **9**, **10**, **13** and **15**, with cisapride[54] (**19**) as the positive control. As shown in **Table 5**, the hERG IC_{50} values of most of the compounds are highger than 10 μM, and compounds **10** and **15** exhibited hERG IC_{50} values higher than 40 μM.

In general, a safe drug candidate is expected to have an hERG IC_{50} value greater than 10 μM,[55, 56] so compound **15** has a relatively low risk of hERG toxicity.

Table 5. hERG inhibitory activity evaluation.

Compound ID	**9**	**10**	**13**	**15**	**19**
hERG IC_{50} (μM)	19.53	> 40	32.85	> 40	0.03

CONCLUSION

CADD has the potential to improve the efficiency of drug research and discovery to assist or accelerate decision making throughout the entire development process. Although an increasing number of successful drug discovery cases involving CADD methods are being reported,[57, 58] the shortcomings of CADD methods are also obvious. For instance, due to inaccurate or inapplicable computational models,[59] the false positive ratio in virtual screenings remains high, and it is still of challenge to reliably prioritize synthetic efforts to focus on the optimization of compounds with favorable activities as well as absorption, distribution, metabolism, excretion, and toxicity properties. The rational application of CADD methods requires experimental researchers to better understand the limitations of computational models and choose the appropriate models by comprehensively considering their computation costs and the expected accuracy level. In this study, we first devised an FGFR-targeted scoring function, the RTKscore, to address the inaccuracy associated with activity rank-ordering of virtual screenings. Based on the RTKscore, we successfully identified compound **8** from a commercial chemical library, and this compound has a novel structure and exhibits sub-nanomolar inhibitory activity (FGFR1 IC_{50} = 114.5 ± 15.3 nM) against FGFR. Structure-guided optimization then led to compound **9** with improved molecular and whole-cell activities against FGFR (FGFR1 IC_{50} = 10.8±1.3 nM, KG1 IC_{50} = 554.4±447.2 nM), and covalent compound **10** with subnanomolar inhibitory activity toward FGFRs and FGFR-dependent cancer cell lines. Molecular biology experiments, X-ray crystallography and protein mass spectrometry studies showed that **10** could selectively target FGFR and form a covalent bond with the Cys residue in the loop of the FGFRs. Despite its excellent *in vitro* activity, compound **10** showed a poor PK profile due to its low solubility in water and metabolic instability issues. To address these problems, we further used site-of-metabolism prediction to identify the metabolically

labile sites on compound **10** and successfully obtained a more soluble and stable compound, **15**. *In vivo* PK experiments indeed showed that **15** has high plasma exposure and an acceptable $t_{1/2}$ when dosing via IP and IV, despite that there was no improvement in oral exposure. Moreover, the hERG inhibitory activity evaluation experiment indicated that **15** has a relatively low risk of hERG toxicity. These results indicated that compound **15** could be a promising FGFR lead compound. Taken together, this study describes our efforts in rational design of novel FGFR inhibitors. Accordingly, further medicinal chemistry exploration around compound **15** is currently ongoing with the aim to provide validated candidates for the novel anticancer treatments.

Experimental Section

RTKscore development

The protocol for the development of the RTKscore is similar to that of SAMscore development. First, we collected the crystal structures of FGFR1 (PDB id: 3TT0), FGFR2 (PDB id: 2PVF), and FGFR3 (PDB id: 4K33) from PDB, and the ligand information for these proteins from the BindingDB, and these data point included the ligand structure and activity information with the corresponding target protein. A total of 1,090 ligands were collected. The activity data of these ligands were converted to pIC50 ($pIC_{50} = 9 - log_{10}(IC_{50})$), and the ligands without explicit data value were marked as inactive with pIC50 = 0. We divided all the ligands into two groups, the training set and the test data in a ratio of 5:1, in which the training data set had 908 ligands and the test data set had 182 ligands.

The molecular docking program Glide was used to generate the binding modes of each ligand with the corresponding target protein. Before molecular docking, the ligands were prepared by the LigPrep module in Schrödinger software (LigPrep, version 3.4; Schrödinger, LLC: New York, NY, 2015), and the protein structures were optimized by the module of Protein Preparation Wizard module in the Maestro program (Maestro, version 10; Schrödinger, LLC: New York, NY, 2015). Based on the optimized protein structures, protein Grid files were generated with the center of the ATP binding site by the Receptor Grid Generation module in the Glide program (Schrödinger, LLC: New York, NY, 2015). The prepared ligand conformations were docked to the corresponding target protein Grid files by Glide with the SP precision mode. All parameters for the above processes were the default parameters. The conformation of the lowest Glide Emodel score for each ligand was selected as the pose of the ligand for further study.

Based on the binding mode of the ligands, the iPMF features for each ligand were calculated with in-house Python scripts for each ligand. Seventeen types of atoms in the proteins, 30 types of atoms in the ligand, and 11 distance ranges (0.0-2.0 Å, 0.0 -3.0 Å, …, and 0.0 – 12.0 Å) were considered. Overall, there were 5610 iPMF features for each ligand. Then, epsilon support vector regression (ε-SVR) and recursive feature elimination (RFE) methods were used to perform feature selection, and the unimportant features were eliminated step by step until the optimal feature sub set of features was identified. The importance of each feature was evaluated by the square of the Pearson correlation coefficient. Fifty unimportant features were eliminated every time, and the data set with sub features were trained with the ε-SVR method and evaluated by 5-fold cross validation (CV). Finally, the model with 1125 features, the RTKscore, was obtained. The RTKscore was compared with Glide on the test data set, and the squares of the correlation efficient of the ligands' pIC_{50} values with the score predicted RTKscore or Glide was calculated.

Virtual screening

The SPECS database, containing 207, 163 compounds, was used as the ligand database for virtual screening. First, we removed compounds containing inorganic atoms, PAINS substructures, low draggability or reactive substructures. After filtering, the remaining 190,038 compounds were prepared using the same protocol used for RTKscore development for virtual screening. The prepared protein structure of FGFR1 (PDB id: 3TT0) from RTKscore development was chosen as the receptor structure for virtual screening. The prepared ligands were docked to the receptor protein structure with Glide, and 5 conformations of each ligand were outputted. Next, we used the RTKscore to evaluate each ligand pose, which included iPMF features calculation, feature selection, and score prediction. According to ligands' scores predicted by the RTKscore, the top 1000 ligands were kept for further analysis. We clustered the ligands into 100 clusters based on fingerprint ECFP4 with software Pipeline Pilot v7.5 software. To ensure selected ligands were structurally diverse, we selected one or two compounds from each cluster. Finally, there were 112 compounds were selected and purchased for biochemical evaluations.

Molecular modeling

For noncovalent inhibitors, the binding mode of the ligand and protein was simulated with the molecular docking program Glide. The protocol of the molecular docking was similar to that mentioned above, and we outputted all conformations of the ligand and checked the conformations manually.

For covalent inhibitors, we simulated their binding mode with CovDock,[60] a covalent docking program from Schrödinger (Schrödinger, LLC: New York, NY, 2015). As the residue Cys488 of the FGFR1 crystal structure (PDB id: 3TT0) was mutated to an alanine, we first mutated the residue 488 back to cystine, and then the protein structure and ligands were prepared with the same protocol as described above. After choosing Cys488 of FGFR1 as the reaction residues of the target protein, and the reaction type was set as a Michael addition reaction. Other parameters were left at the default settings.

General chemistry information

As shown in schemes 1, we developed an efficient route to obtain derivatives **8-16**. Herein, we use 2'-hydroxyacetophenone derivatives **17a-d** as the starting materials (Scheme 1) and treated them with ethyl bromoacetate and K_2CO_3 in DMF to obtain the intermediates **19a-d**. Subsequent treatment with **21a-c** to afforded the pyrazole intermediates **22a-f**. Compounds **8, 9,** and **23a-d** were synthesized by the reaction of intermediates **22a-f** and hydrazine hydrate in EtOH under one-pot conditions. The reductions of compounds **23a-c** with Fe powder afforded the aniline derivatives, which were ideally poised to undergo acylation with the corresponding acyl chlorides to afford compounds **10** and **12-16**. The Cbz group of **23d** was deprotected by $Pd(OH)_2/H_2$ in MeOH to generate the amine intermediate, which could then undergo acylation with acryloyl chloride to afford compound **11**.

Scheme 1 [a]

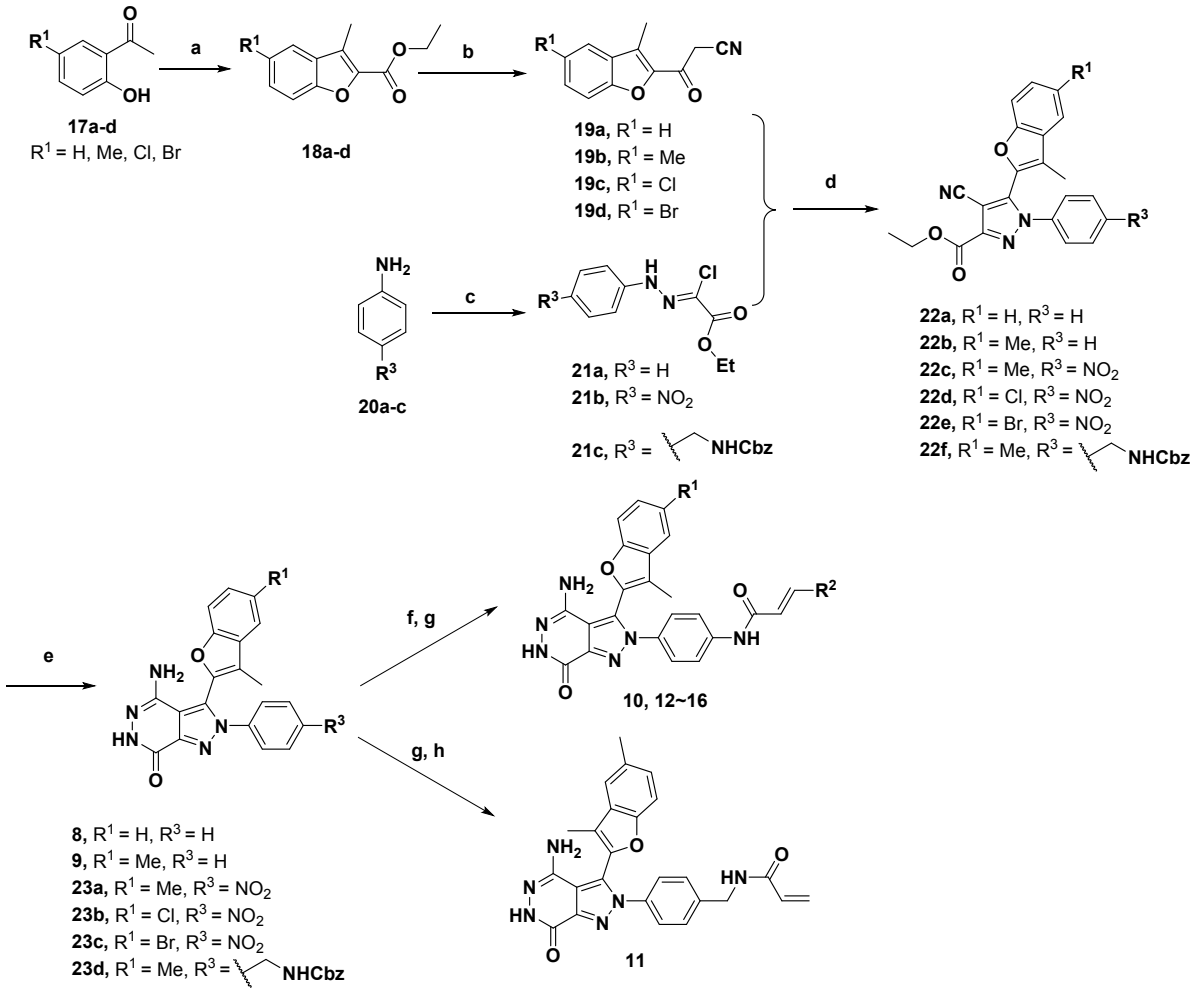

[a]Reagents and conditions: (a) Ethyl bromoacetate, K_2CO_3, DMF, 100 °C; (b) CH_3CN, NaH, THF, 50 °C; (c) Ethyl 2-chloroacetoacetate, $NaNO_2$, NaOAc, EtOH, H_2O/HCl (3:1, v/v), 0 °C-rt; (d) Et_3N, DCM, rt; (e) $N_2H_4{\cdot}H_2O$, HCl (conc.), EtOH, 100 °C, MW; (f) For compunds **23a-c**, Fe, HCl (conc.), MeOH/H_2O (6:1, v/v), 80 °C, 1 h; (g) Acryloyl chloride or acryloyl chloride amino derivatives, K_2CO_3, THF, rt; (h) For compund **23d**, $Pd(OH)_2$/C, HCl (conc.), MeOH, 40 °C, 8 h.

General methods.

The reagents (chemicals) were purchased and used without further purification. Nuclear magnetic resonance (NMR) spectroscopy was performed on a Bruker AMX-400 and AMX-300 NMR (TMS as the IS). Chemical shifts are reported in parts per million (ppm, δ) downfield from TMS. Proton coupling patterns are described as singlet (s), doublet (d), triplet (t), quartet (q), and multiplet (m). Low- and high-resolution mass spectra (LRMS and HRMS) were acquired with electron impact, electrospray, and matrix-assisted laser desorption ionization (EI, ESI, and MALDI) analyses on a Finnigan MAT-95, LCQ-DECA spectrometer and an IonSpec 4.7 T instrument. HPLC analyses of all final compounds for biological testing were carried out on an Agilent 1260 Series HPLC with an Agilent Extend-C18 column (150×4.6 mm, 5 μm) (**Table S5**). All final compounds achieved a minimum of 95% purity. The known acryloyl chloride amino derivatives were already prepared.[61]

4-Amino-3-(3-methylbenzofuran-2-yl)-2-phenyl-2,6-dihydro-7*H*-pyrazolo[3,4-*d*]pyridazin-7-one (8).

To a solution of **22a** (500 mg, 1.35 mmol) in EtOH (5 mL) was added hydrazine hydrate (472 mg, 9.42 mmol). The mixture was stirred at 60 °C overnight. The reaction mixture was diluted with water (20

mL). The reaction mixture was then extracted with DCM (3 × 30 mL), and the combined organic layers were dried over Na_2SO_4 and concentrated under reduced pressure. The residue was dissolved in EtOH (5 mL) and added few drops HCl (con.). The mixture was stirred at 100 °C for 2 h under microwave irradiation. The reaction mixture was then concentrated under reduced pressure and purified by column chromatography using silica with 10% MeOH in DCM as eluent to give **8** (210 mg, 32% yield), as a yellow solid. ^{1}H NMR (500 MHz, DMSO-d_6) δ 11.48 (s, 1H), 7.66 (d, J = 7.5 Hz, 1H), 7.59 (d, J = 8.3 Hz, 1H), 7.50 – 7.39 (m, 6H), 7.36 – 7.30 (m, 1H), 5.20 (s, 2H), 1.92 (s, 3H). ^{13}C NMR (126 MHz, DMSO) δ 155.00, 154.47, 143.19, 143.11, 138.92, 137.37, 129.44, 128.61, 127.63, 126.19, 124.65, 123.22, 120.64, 119.85, 114.82, 111.54, 8.12. LRMS (ESI, m/z): 358.0 $[M+H]^+$; HRMS (ESI) m/z: cacld for $C_{20}H_{15}N_5O_2$ ($[M+H]^+$): 358.1299; found: 358.1290.

4-Amino-3-(3,5-dimethylbenzofuran-2-yl)-2-phenyl-2,6-dihydro-7*H*-pyrazolo[3,4-*d*]pyridazin-7-one (9).

Compound **9** was prepared in a similar manner as described for compound **8**. Yield: 31%. ^{1}H NMR (500 MHz, DMSO-d_6) δ 11.49 (s, 1H), 7.52 – 7.36 (m, 7H), 7.26 – 7.17 (m, 1H), 5.19 (s, 2H), 3.07 (s, 3H), 1.87 (s, 3H). ^{13}C NMR (126 MHz, DMSO-d_6) δ 155.02, 152.94, 143.21, 143.10, 138.92, 137.43, 132.44, 129.46, 129.41, 128.67, 127.74, 127.39, 124.60, 120.25, 119.59, 114.76, 111.12, 20.86, 8.11. LRMS (ESI, m/z): 372.0 $[M+H]^+$; HRMS (ESI) m/z: cacld for $C_{21}H_{17}N_5O_2$ ($[M+Na]^+$): 394.1274; found: 394.1272.

***N*-(4-(4-Amino-3-(3,5-dimethylbenzofuran-2-yl)-7-oxo-6,7-dihydro-2*H*-pyrazolo[3,4-*d*]pyridazin-2-yl)phenyl)acrylamide (10).**

To a solution of **23a** (500 mg, 1.2 mmol) in MeOH/H_2O (6:1, 14 mL) was added HCl (0.5 mL) and Fe powder (268 mg, 4.8 mmol). The mixture was stirred at 80 °C for 6 h. The reaction mixture was filtered and the filtrate was concentrated under reduced pressure. The residue was dissolved in THF (5 mL) and added K_2CO_3 (248.8 mg, 1.8 mmol). Then a solution of acryloyl chloride (217.2 mg, 2.4 mmol) in THF (5 mL) was added to the reaction mixture dropwise at rt. Until TLC showed the reaction completed, the reaction mixture was then concentrated under reduced pressure and purified by column chromatography using silica with 10% MeOH in DCM as eluent to give **10** (120 mg, 23% yield), as a yellow solid. ^{1}H NMR (400 MHz, DMSO-d_6) δ 11.48 (s, 1H), 10.95 (s, 1H), 7.82 (d, J = 8.9 Hz, 2H), 7.55 – 7.32 (m, 4H), 7.22 (d, J = 8.9 Hz, 1H), 6.59 (dd, J = 17.0, 10.2 Hz, 1H), 6.25 (d, J = 17.0 Hz, 1H), 5.75 (d, J = 10.2 Hz, 1H), 5.19 (s, 2H), 2.41 (s, 3H), 1.89 (s, 3H). ^{13}C NMR (126 MHz, DMSO-d_6) δ 163.55, 155.00, 152.93, 143.17, 142.91, 140.04, 137.48, 133.82, 132.40, 131.78, 128.67, 127.58, 127.34, 127.15, 125.05, 120.25, 119.47, 114.61, 111.11, 20.86, 8.14. LRMS (ESI, m/z): 441.9 $[M+H]^+$; HRMS (ESI) m/z: cacld for $C_{24}H_{21}N_6O_3$ ($[M+H]^+$): 441.1670; found: 441.1681.

***N*-(4-(4-Amino-3-(3,5-dimethylbenzofuran-2-yl)-7-oxo-6,7-dihydro-2*H*-pyrazolo[3,4-*d*]pyridazin-2-yl)benzyl)acrylamide (11).**

To a solution of **23d** (540 mg, 1.0 mmol) in MeOH (5 mL) was added HCl (1 mL) and $Pd(OH)_2/C$ (20%, 35 mg, 0.05 mmol). The mixture was stirred at 40 °C overnight under H_2 atmosphere. The reaction mixture was filtered and the filtrate was concentrated under reduced pressure. The residue was dissolved in THF (5 mL) and added K_2CO_3 (207.3 mg, 1.5 mmol). Then a solution of acryloyl chloride (181 mg, 2 mmol) in THF (5 mL) was added to the reaction mixture dropwise at rt. Until TLC showed the reaction completed, the reaction mixture was then concentrated under reduced pressure and purified by column chromatography using silica with 10% MeOH in DCM as eluent to give **11** (99 mg, 21% yield), as a yellow solid. ^{1}H NMR (400 MHz, DMSO-d_6) δ 11.51 (s, 1H), 8.82 (t, J = 5.9 Hz, 1H), 7.48 (d, J = 8.4 Hz, 1H), 7.45 – 7.38 (m, 3H), 7.32 (d, J = 8.5 Hz, 2H), 7.22 (d, J = 8.6 Hz, 1H), 6.30 (dd, J = 17.1, 10.2 Hz, 1H), 6.12 (dd, J = 17.1, 2.0 Hz, 1H), 5.61 (dd, J = 10.2, 2.0 Hz, 1H), 5.19 (s, 2H), 4.37 (d, J = 6.0 Hz, 2H), 2.40 (s, 3H), 1.89 (s, 3H). ^{13}C NMR (126 MHz, DMSO-d_6) δ 164.88, 155.09, 153.01, 143.26, 143.06, 140.81, 137.66, 137.42, 132.52, 131.52, 128.70, 128.06, 127.70, 127.46, 125.78, 124.56, 120.32, 119.69, 114.86, 111.22, 41.54, 20.91, 8.19. LRMS (ESI, m/z): 456.0 $[M+H]^+$; HRMS (ESI) m/z: cacld for $C_{25}H_{23}N_6O_3$ ($[M+H]^+$): 455.1826; found: 455.1837.

_N_-(4-(4-Amino-3-(5-chloro-3-methylbenzofuran-2-yl)-7-oxo-6,7-dihydro-2_H_-pyrazolo[3,4-_d_]pyridazin-2-yl)phenyl)acrylamide (12)

Compound **12** was prepared in a similar manner as described for compound **10**. Yield: 20%. ^{1}H NMR (400 MHz, DMSO-d_6) δ 11.50 (s, 1H), 10.43 (s, 1H), 7.82 – 7.69 (m, 3H), 7.64 (d, J = 8.8 Hz, 1H), 7.45 – 7.38 (m, 3H), 6.43 (dd, J = 17.0, 10.1 Hz, 1H), 6.26 (d, J = 17.0 Hz, 1H), 5.78 (d, J = 11.2 Hz, 1H), 5.23 (s, 2H), 1.95 (s, 3H). ^{13}C NMR (126 MHz, DMSO-d_6) δ 163.45, 154.95, 153.03, 143.17, 142.99, 139.85, 139.00, 133.88, 131.53, 130.38, 127.71, 127.56, 126.98, 125.98, 125.23, 120.29, 119.79, 119.57, 114.86, 113.23, 8.17. LRMS (ESI, m/z): 461.0 [M+H]$^+$; HRMS (ESI) m/z: cacld for $C_{23}H_{17}N_6O_3Cl$ ([M+Na]$^+$): 483.0943; found: 483.0952.

(_E_)-_N_-(4-(4-Amino-3-(3,5-dimethylbenzofuran-2-yl)-7-oxo-6,7-dihydro-2_H_-pyrazolo[3,4-_d_]pyridazin-2-yl)phenyl)-4-(dimethylamino)but-2-enamide (13).

Compound **13** was prepared in a similar manner as described for compound **10**. Yield: 19%. ^{1}H NMR (400 MHz, DMSO-d_6) δ 11.48 (s, 1H), 10.61 (s, 1H), 7.80 – 7.71 (m, 2H), 7.49 – 7.37 (m, 4H), 7.23 (dd, J = 8.5, 1.6 Hz, 1H), 6.76 (d, J = 15.4 Hz, 1H), 6.38 (d, J = 15.4 Hz, 1H), 5.18 (s, 2H), 2.41 (s, 3H), 2.36 (s, 6H), 1.89 (s, 3H). ^{13}C NMR (126 MHz, DMSO-d_6) δ 163.21, 155.08, 152.99, 143.25, 142.97, 139.95, 137.51, 133.94, 132.49, 128.72, 127.67, 127.41, 125.21, 120.29, 119.55, 114.67, 111.17, 58.66, 44.04, 20.91, 8.20. HRMS (ESI) m/z: cacld for $C_{27}H_{26}N_7O_3$ ([M-H]$^-$): 496.2103; found: 496.2109.

(_E_)-_N_-(4-(4-Amino-3-(3,5-dimethylbenzofuran-2-yl)-7-oxo-6,7-dihydro-2_H_-pyrazolo[3,4-_d_]pyridazin-2-yl)phenyl)-4-morpholinobut-2-enamide (14).

Compound **14** was prepared in a similar manner as described for compound **10**. Yield: 9%. ^{1}H NMR (400 MHz, DMSO-d_6) δ 11.48 (s, 1H), 10.41 (s, 1H), 7.74 (d, J = 9.0 Hz, 2H), 7.49 (d, J = 8.4 Hz, 1H), 7.44 (s, 1H), 7.41 – 7.36 (m, 2H), 7.23 (dd, J = 8.5, 1.6 Hz, 1H), 6.79 – 6.70 (m, 1H), 6.33 (d, J = 15.1 Hz, 1H), 5.19 (s, 2H), 3.72 – 3.57 (m, 4H), 3.29 – 3.11 (m, 2H), 2.49 – 2.30 (m, 7H), 1.90 (s, 3H). ^{13}C NMR (126 MHz, DMSO-d_6) δ 162.32, 155.00, 152.93, 143.16, 142.93, 139.88, 137.48, 133.87, 132.40, 128.69, 127.59, 127.33, 125.18, 120.23, 119.51, 119.46, 114.62, 111.12, 66.00, 52.99, 45.66, 20.86, 8.15. HRMS (ESI) m/z: cacld for $C_{29}H_{28}N_7O_4$ ([M-H]$^-$): 538.2208; found: 538.2211.

(_E_)-_N_-(4-(4-Amino-3-(5-chloro-3-methylbenzofuran-2-yl)-7-oxo-6,7-dihydro-2_H_-pyrazolo[3,4-_d_]pyridazin-2-yl)phenyl)-4-(dimethylamino)but-2-enamide (15).

Compound **15** was prepared in a similar manner as described for compound **10**. Yield: 25%. ^{1}H NMR (400 MHz, DMSO-d_6) δ 11.49 (s, 1H), 10.70 (s, 1H), 7.80 – 7.73 (m, 3H), 7.64 (d, J = 8.8 Hz, 1H), 7.49 – 7.31 (m, 3H), 6.83 – 6.73 (m, 1H), 6.47 (d, J = 15.4 Hz, 1H), 5.23 (s, 2H), 3.92 (d, J = 6.8 Hz, 2H), 2.75 (s, 6H), 1.95 (s, 3H). ^{13}C NMR (126 MHz, DMSO) δ 162.32, 154.92, 153.03, 143.14, 142.99, 139.67, 138.97, 134.05, 131.54, 130.38, 127.69, 126.98, 125.97, 125.27, 120.28, 119.79, 119.68, 114.85, 113.22, 56.64, 41.92, 8.16. HRMS (ESI) m/z: cacld for $C_{26}H_{25}ClN_7O_3$ ([M+H]$^+$): 518.1702; found: 518.1707.

(_E_)-_N_-(4-(4-Amino-3-(5-bromo-3-methylbenzofuran-2-yl)-7-oxo-6,7-dihydro-2_H_-pyrazolo[3,4-_d_]pyridazin-2-yl)phenyl)-4-(dimethylamino)but-2-enamide (16).

Compound **16** was prepared in a similar manner as described for compound **10**. Yield: 14%. ^{1}H NMR (400 MHz, DMSO-d_6) δ 11.50 (s, 1H), 11.02 (s, 1H), 7.92 (d, J = 5.1 Hz, 1H), 7.82 (d, J = 9.0 Hz, 2H), 7.58 – 7.52 (m, 2H), 7.42 – 7.34 (m, 2H), 6.86 – 6.77 (m, 1H), 6.55 (d, J = 15.4 Hz, 1H), 5.23 (s, 3H), 3.73 (d, J = 5.7 Hz, 2H), 2.61 (s, 6H), 1.94 (s, 3H). ^{13}C NMR (126 MHz, DMSO-d_6) δ 162.77, 155.01, 153.42, 143.23, 143.00, 140.00, 138.80, 133.90, 130.99, 128.71, 127.01, 125.20, 124.80, 123.33, 121.59, 119.72, 119.64, 115.59, 114.88, 113.72, 57.27, 42.51, 8.19. HRMS (ESI) m/z: cacld for $C_{26}H_{25}N_7O_3Br$ ([M+H]$^+$): 562.1197; found: 562.1210.

Ethyl 3-methylbenzofuran-2-carboxylate (18a).

To a solution of 2'-hydroxyacetophenone **17a** (2.0 g, 14.4 mmol) in dry DMF (20 mL) was added K_2CO_3 (2.98 g, 21.6 mmol) and ethyl bromoacetate (2.88 g, 17.3 mmol), respectively. The mixture was stirred at 100 °C overnight under Ar. The reaction mixture was then cooled to rt. The suspension was filtered through a Celite cartridge, and the cartridge rinsed with EA. The filtrate was diluted with EA and water. The reaction mixture was then extracted with EA (3 × 40 mL), and the combined organic layers were dried over Na_2SO_4 and concentrated under reduced pressure. The residue was purified by column chromatography on silica gel with using 5% EA in hexane as eluent to give **18a** (1.8 g, 61% yield), as a white solid. ^{1}H NMR (400 MHz, $CDCl_3$) δ 7.64-7.62 (m, 1H), 7.56-7.52 (m, 1H), 7.46-7.42 (m, 1H), 7.32-7.26 (m, 1H), 4.45 (q, *J* = 7.1 Hz, 2H), 2.59 (s, 3H), 1.44 (t, *J* = 7.1 Hz, 3H).

Ethyl 3,5-dimethylbenzofuran-2-carboxylate (18b).

Compound **12b** was prepared in a similar manner as described for compound **11a**. Yield: 41%. ^{1}H NMR (400 MHz, $CDCl_3$) δ 7.45 – 7.34 (m, 2H), 7.27 – 7.21 (m, 1H), 4.44 (q, *J* = 7.1 Hz, 2H), 2.56 (s, 3H), 2.46 (s, 3H), 1.44 (t, *J* = 7.1 Hz, 3H).

Ethyl 5-chloro-3-methylbenzofuran-2-carboxylate (18c).

Compound **12c** was prepared in a similar manner as described for compound **11a**. Yield: 43%. ^{1}H NMR (400 MHz, $CDCl_3$) δ 7.60 (d, *J* = 2.1 Hz, 1H), 7.47 (d, *J* = 8.8 Hz, 1H), 7.39 (dd, *J* = 8.8, 2.1 Hz, 1H), 4.45 (q, *J* = 7.1 Hz, 2H), 2.56 (s, 3H), 1.44 (t, *J* = 7.1 Hz, 3H).

Ethyl 5-bromo-3-methylbenzofuran-2-carboxylate (18d).

Compound **12d** was prepared in a similar manner as described for compound **11a**. Yield: 45%. ^{1}H NMR (400 MHz, $CDCl_3$) δ 7.76 (d, *J* = 1.8 Hz, 1H), 7.52 (dd, *J* = 8.8, 1.8 Hz, 1H), 7.42 (d, *J* = 8.8 Hz, 1H), 4.45 (q, *J* = 7.1 Hz, 2H), 2.55 (s, 3H), 1.44 (t, *J* = 7.1 Hz, 3H).

3-(3-Methylbenzofuran-2-yl)-3-oxopropanenitrile (19a).

To a solution of ethyl 3-methyl-2-benzofurancarboxylate **11a** (2 g, 9.79 mmol) and acetonitrile (1.0 mL, 19.6 mmol) in dry THF (25 mL) was added sodium hydride (60%, 0.51 g, 12.7 mmol) portionwise. The resulting mixture was stirred at 50 °C for 8 h under Ar, and then allowed to cool to room temperature. The mixture was quenched with saturated ammonium chloride solution (50 mL) and then was acidified with 1N HCl solution until pH 5-6. The resulting precipitate was filtered, washed with water, and dried to afford **12a** (1.3 g) as a pale-yellow solid. The compound was used without further purification. LRMS (ESI, m/z): 198.1 $[M-H]^-$.

3-(3,5-Dimethylbenzofuran-2-yl)-3-oxopropanenitrile (19b)

Compound **19b** was prepared in a similar manner as described for compound **19a**. Yield: 73%. LRMS (ESI, m/z): 212.0 $[M-H]^-$.

3-(5-Chloro-3-methylbenzofuran-2-yl)-3-oxopropanenitrile (19c)

Compound **19c** was prepared in a similar manner as described for compound **19a**. Yield: 45%. LRMS (ESI, m/z): 233.0 $[M-H]^-$.

3-(5-Bromo-3-methylbenzofuran-2-yl)-3-oxopropanenitrile (19d)

Compound **19d** was prepared in a similar manner as described for compound **19a**. Yield: 38%. LRMS (ESI, m/z): 277.1 $[M-H]^-$.

(*Z*)-Ethyl 2-chloro-2-(2-phenylhydrazono)acetate (21a).

To a solution of aniline (5.0 g, 52.08 mmol) in 3M HCl (40 mL) at 0 °C was added a solution of sodium nitrite (3.95 g, 57.3 mmol) in water (10 mL) dropwise. The mixture was stirred at 0°C for 1 h, then a solution of NaOAc (4.7 g, 57.3 mmol) and ethyl 2-chloroacetoacetate (9.43 g, 57.3 mmol) in EtOH (30 mL) was added and the mixture was stirred at rt for 4 h. The reaction was quenched with water (50 mL),

then extracted with EA (3 × 40 mL), and the combined organic layers were dried over Na_2SO_4 and concentrated under reduced pressure. The residue was purified by column chromatography using silica with 10% EtOAc in hexane as eluent to give **21a** (9 g, 76% yield), as a yellow solid. ^{1}H NMR (400 MHz, $CDCl_3$) δ 8.33 (s, 1H), 7.37 – 7.31 (m, 2H), 7.25 – 7.21 (m, 2H), 7.08 – 7.01 (m, 1H), 4.39 (q, *J* = 7.1 Hz, 2H), 1.41 (t, *J* = 7.1 Hz, 3H).

(*Z*)-Ethyl 2-chloro-2-(2-(4-nitrophenyl)hydrazono)acetate (21b)

Compound **21b** was prepared in a similar manner as described for compound **21a**. Yield: 82%。 ^{1}H NMR (400 MHz, $CDCl_3$) δ 8.62 (s, 1H), 8.30 – 8.17 (m, 2H), 7.35 – 7.28 (m, 2H), 4.41 (q, *J* = 7.1 Hz, 2H), 1.42 (t, *J* = 7.1 Hz, 3H).

(*Z*)-Ethyl 2-(2-(4-((((benzyloxy)carbonyl)amino)methyl)phenyl)hydrazono)-2-chloroacetate (21c).

Compound **21c** was prepared in a similar manner as described for compound **21a**. Yield: 60%。 LRMS (ESI, m/z): 413.0 $[M+Na]^+$.

Ethyl 4-cyano-5-(3-methylbenzofuran-2-yl)-1-phenyl-1*H*-pyrazole-3-carboxylate (22a).

To a solution of **19a** (1.0 g, 4.6 mmol) in DCM (10 mL) was added NEt_3 (1.86 g, 18.4 mmol) and **21a** (1.25 g, 5.5 mmol), respectively. The mixture was stirred at rt for 5 h. The reaction mixture was diluted with water (30 mL). The reaction mixture was then extracted with EA (3 × 30 mL), and the combined organic layers were dried over Na_2SO_4 and concentrated under reduced pressure. The residue was purified by column chromatography using silica with 15% EA in hexane as eluent to give **22a** (1.0 g, 56% yield), as a yellow solid. **^{1}H NMR (400 MHz, $CDCl_3$)** δ 7.51 (dd, *J* = 8.5, 5.3 Hz, 1H), 7.39 (s, 5H), 7.11 – 7.03 (m, 2H), 4.54 (q, *J* = 7.1 Hz, 2H), 2.26 (s, 3H), 1.48 (t, *J* = 7.1 Hz, 3H).

Ethyl 4-cyano-5-(3,5-dimethylbenzofuran-2-yl)-1-phenyl-1*H*-pyrazole-3-carboxylate (22b).

Compound **22b** was prepared in a similar manner as described for compound **22a**. Yield: 43%。 ^{1}H NMR (400 MHz, **$CDCl_3$**) δ 7.41 – 7.35 (m, 5H), 7.24 – 7.15 (m, 3H), 4.54 (q, *J* = 7.1 Hz, 2H), 2.46 (s, 3H), 2.23 (s, 3H), 1.48 (t, *J* = 7.1 Hz, 3H).

Ethyl 4-cyano-5-(3,5-dimethylbenzofuran-2-yl)-1-(4-nitrophenyl)-1*H*-pyrazole-3-carboxylate (22c).

Compound **22c** was prepared in a similar manner as described for compound **22a**. Yield: 41%。 ^{1}H NMR (400 MHz, DMSO-d_6) δ 8.39 – 8.30 (m, 2H), 7.79 – 7.69 (m, 2H), 7.57 – 7.52 (m, 1H), 7.38 (d, *J* = 8.5 Hz, 1H), 7.25 (dd, *J* = 8.5, 1.7 Hz, 1H), 4.45 (q, *J* = 7.1 Hz, 2H), 2.42 (s, 3H), 2.21 (s, 3H), 1.37 (t, *J* = 7.1 Hz, 3H).

Ethyl 5-(5-chloro-3-methylbenzofuran-2-yl)-4-cyano-1-(4-nitrophenyl)-1*H*-pyrazole-3-carboxylate (22d).

Compound **22d** was prepared in a similar manner as described for compound **22a**. Yield: 46%。 LRMS (ESI, m/z): 450.0 $[M-H]^-$.

Ethyl 5-(5-bromo-3-methylbenzofuran-2-yl)-4-cyano-1-(4-nitrophenyl)-1H-pyrazole-3-carboxylate (22e).

Compound **22e** was prepared in a similar manner as described for compound **22a**. Yield: 36%。 ^{1}H NMR (400 MHz, **$CDCl_3$**) δ 7.52 – 7.47 (m, 2H), 7.40 – 7.37 (m, 1H), 7.30 – 7.26 (m, 2H), 7.23 (s, 1H), 7.22 – 7.18 (m, 1H), 4.54 (q, *J* = 7.1 Hz, 2H), 2.47 (s, 3H), 2.29 (s, 3H), 1.48 (t, *J* = 7.1 Hz, 3H).

Ethyl 1-(4-((((benzyloxy)carbonyl)amino)methyl)phenyl)-4-cyano-5-(3,5-dimethylbenzofuran-2-yl)-1*H*-pyrazole-3-carboxylate (22f).

Compound **22f** was prepared in a similar manner as described for compound **22a**. Yield: 55%。^{1}H NMR (400 MHz, **$CDCl_3$**) δ 7.41 – 7.27 (m, 11H), 7.24 – 7.16 (m, 2H), 5.12 (s, 2H), 4.54 (q, *J* = 7.1 Hz, 2H), 4.40 (d, *J* = 6.0 Hz, 2H), 2.47 (s, 3H), 2.24 (s, 3H), 1.48 (t, 3H).

4-Amino-3-(3,5-dimethylbenzofuran-2-yl)-2-(4-nitrophenyl)-2,6-dihydro-7*H*-pyrazolo[3,4-d]pyridazin-7-one (23a).

Compound **23a** was prepared in a similar manner as described for compound **8**. Yield: 32%. ^{1}H NMR (400 MHz, DMSO-d_6) δ 11.55 (s, 1H), 8.35 – 8.28 (m, 2H), 7.76 – 7.69 (m, 2H), 7.52 – 7.44 (m, 2H), 7.25 (dd, *J* = 8.5, 1.3 Hz, 1H), 5.27 (s, 2H), 2.42 (s, 3H), 1.94 (s, 3H).

4-Amino-3-(5-chloro-3-methylbenzofuran-2-yl)-2-(4-nitrophenyl)-2,6-dihydro-7*H*-pyrazolo[3,4-*d*]pyridazin-7-one (23b).

Compound **23b** was prepared in a similar manner as described for compound **8**. Yield: 44%. LRMS (ESI, m/z): 458.8 $[M+Na]^+$.

4-Amino-3-(5-bromo-3-methylbenzofuran-2-yl)-2-(4-nitrophenyl)-2,6-dihydro-7*H*-pyrazolo[3,4-*d*]pyridazin-7-one (23c).

Compound **23c** was prepared in a similar manner as described for compound **8**. Yield: 26%. LRMS (ESI, m/z): 480.8, 482.7 $[M, M+2]^+$.

Benzyl (4-(4-amino-3-(3,5-dimethylbenzofuran-2-yl)-7-oxo-6,7-dihydro-2*H*-pyrazolo[3,4-*d*]pyridazin-2-yl)benzyl)carbamate (23d).

Compound **23d** was prepared in a similar manner as described for compound **8**. Yield: 28%. ^{1}H NMR (400 MHz, DMSO-d_6) δ 11.49 (s, 1H), 7.87 (t, *J* = 6.1 Hz, 1H), 7.49 (d, *J* = 8.4 Hz, 1H), 7.45 – 7.37 (m, 3H), 7.35 – 7.28 (m, 6H), 7.23 (d, *J* = 8.5 Hz, 1H), 5.17 (s, 2H), 5.03 (s, 2H), 4.23 (d, *J* = 6.1 Hz, 2H), 2.41 (s, 3H), 1.88 (s, 3H).

Kinase inhibition assay

FGFR1, FGFR2, FGFR3, FGFR4, VEGFR2, VEGFR1, PDGFRβ, Ret, c-Src and c-Met active proteins were purchased from Eurofins. The kinase activities were assessed using ELISA assay. Briefly, 96-well plates were precoated with 20 μg/mL poly (Glu, Tyr) $_{4:1}$ (Sigma, St Louis, MO, USA) as a substrate. A 50-μL aliquot of 10 μmol/L ATP solution diluted in kinase reaction buffer (50 mmol/L HEPES [pH 7.4], 50 mmol/L $MgCl_2$, 0.5 mmol/L $MnCl_2$, 0.2 mmol/L Na_3VO_4, and 1 mmol/L DTT) was added to each well; 1 μL of the indicated compound diluted in 1% DMSO (v/v) (Sigma, St. Louis, MO, USA) was then added to each reaction well. DMSO (1%, v/v) was used as the negative control. The kinase reaction was initiated by the addition of purified tyrosine kinase proteins diluted in 49 μL of kinase reaction buffer. After incubation for 60 min at 37 °C, the plate was washed three times with phosphate-buffered saline (PBS) containing 0.1% Tween 20 (T-PBS). Antiphosphotyrosine (PY99) antibody (100 μL; 1:500, diluted in 5 mg/mL BSA T-PBS) was then added. After a 30-min incubation at 37 °C, the plate was washed three times, and 100 μL of horseradish peroxidase-conjugated goat anti-mouse IgG (1:1000, diluted in 5 mg/mL BSA T-PBS) was added. The plate was then incubated at 37 °C for 30 min and washed 3 times. A 100-μL aliquot of a solution containing 0.03% H_2O_2 and 2 mg/mL o-phenylenediamine in 0.1 mol/L citrate buffer (pH 5.5) was then added. The reaction was terminated by the addition of 50 μL of 2 mol/L H_2SO_4, causing a color, and the plate was then analyzed using a multiwell spectrophotometer (SpectraMAX190, from Molecular Devices, Palo Alto, CA, USA) at 490 nm. The inhibition rate (%) was calculated using the following equation: [1-(A490/A490 control)] ×100%. The IC_{50} values were calculated from the inhibition curves in two separate experiments.

Kinase kinetic inhibition assessment

Kinetics of Inhibition Assays for irreversible inhibition as well as Ki, Kinact, and Kinact/Ki calculation was conducted in Shanghai ChemPartner Co., Ltd (China).

Cell culture

Unless otherwise mentioned, the cells were purchased from American Type Culture Collection (ATCC). RT112 was obtained from Deutsche Sammlung von Mikroorganismen und Zellkulturen GmbH (DSMZ). UMUC14 was obtained from the European Collection of Cell Cultures (ECACC). SUM52PE was obtained from Asterand Company. All the cell lines used in this study were obtained between 2000 and 2017 and cultured according to the suppliers' instructions. Cells were checked to confirmed to be mycoplasma free, and the cells were passaged no more than 25-30 times after thawing. Cell lines were characterized by Genesky Biopharma Technology using short tandem repeat markers (latest tested in 2017).

Western blot analysis

Cells were treated with the indicated dose of the test compounds for 2 h at 37 °C and then lysed in 1×SDS sample buffer. The cell lysates were subsequently resolved by 10% SDS-PAGE and transferred to nitrocellulose membranes. The membranes were probed with the appropriate primary antibodies and then with horseradish peroxidase-conjugated anti-rabbit or anti-mouse IgG. The immune reactive proteins were detected using an enhanced chemiluminescence detection reagent (Thermo Fisher Scientific, Rockford, IL, USA).

Cell proliferation assays

Cells were seeded in 96-well plates at a low density in growth medium. The next day, the appropriate controls or designated concentrations of test compounds were added to each well, and the cells were incubated for 72 h. Finally, cell proliferation was determined using a sulforhodamine B (SRB) assay or a cell counting kit (CCK-8) assay. The IC_{50} values were calculated by fitting concentration-response curves fitting using a SoftMax pro-based four-parameter method.

Protein purification and crystallization

The kinase domain (residues 458-756, with mutagenesis of C488A and C584S） of recombinant human FGFR1 was produced following the protocol we have published previously.[62] Crystallization of the FGFR1 kinase domain was carried out by mixing a solution of the protein with an equal volume of precipitation solution (0.1 M Bis-Tris pH 6.5, 0.3 M $(NH4)_2SO_4$, 5% glycerol, 15-20% PEG10K). Crystallization utilized the vapor-diffusion method in hanging drops at 4 ℃. Crystals appeared in one week. The crystals of the protein-ligand complex were obtained by soaking the apo crystals in a buffer (0.1 M Bis-Tris, pH 6.5, 0.3 M $(NH4)_2SO_4$, 5% glycerol, 25% PEG10K) containing 1 mM inhibitor compound **9**. Crystals of the complex were then flash frozen in liquid nitrogen in the presence of soaking buffer.

The human FGFR4 kinase domain (residues 445-753, R664E) was expressed and purified as follows. The cDNA fragment was cloned into the pET28a vector at NcoI/XhoI restriction sites. Then the construct was coexpressed with catYopH subcloned in pET15b (164-468 aa).[63] The expressed protein was passed through a Ni-NTA column (Qiagen). The kinase domain was further purified on a Q HP ion exchange column (GE) which eluted with 20 mM Tris at pH 7.5 with 150 mM NaCl, 10% glycerol, 1 mM DTT. The eluted protein was buffer exchanged into 10 mM HEPES at pH 8.0 with 100mM NaCl, 3% glycerol, 1 mM TCEP using a HiLoad 16/ 60 Superdex^{TM} 75 column (GE Health). The protein was concentrated to ~ 10-20 mg/mL for further crystallization. Cocrystal of the FGFR4 kinase domain with different compounds were obtained by vapor-diffusion in a reservoir solution of 0.1 M MES at pH 5.5 with 0.2 M Li_2SO_4, 18% PEG3350 for compound **10** and 0.1 M HEPES at pH 7.5 with 1.3 M $(NH4)_2SO_4$ for compound **11**, respectively.

Structure determination and refinement

Data were collected at 100 K at the Shanghai Synchrotron Radiation Facility (SSRF) and were processed with the XDS[64] and HKL3000[65] software packages. The structures were solved by molecular replacement using the program PHASER[66] with the search model of PDB codes 5Z0S[62] for FGFR1 and 4QQT[67] for FGFR4. The structures were refined with the simulated-annealing protocol implemented in the program PHENIX.[68] With the aid of the program Coot,[69] the compound, as well as water molecules, were fitted into an initial F_o-F_c map. The refined structures were deposited in Protein Data Bank with accession codes 6ITJ for compound **9**, 6IUP for compound **10**, and 6IUO for compound **11**. The complete statistics, as well as the qualities of the solved structures, are shown in **Table S2**.

HPLC–MS/MS analysis

The human FGFR4 kinase domain was produced by following the protocol described above and was included in the buffer of 10 mM HEPES at pH 8.0 with 100 mM NaCl and 3% glycerol. The FGFR4 kinase domain protein was incubated with 1 mg/mL compound **10** at 4 °C for 24 h, and then preseparated by SDS-PAGE and cut off from the PAGE gel. Next, the protein was incubated with trypsin (trypsin: protein = 1:50 (w/w)) at 37 °C for 20 h. The tryptic peptides were desalted and dried in a Speed-Vac. The peak lists from HPLC–MS/MS data were generated by Proteome Discoverer software (version 1.4, Thermo Fisher) and searched against the UniProt Human database by Mascot (v2.3, Matrix Science Ltd., London, UK). Two kinds of mass spectrometry, higher energy collision dissociation mass spectrometry and collision-induced dissociation mass spectrometry, were used to identify the modification of the human FGFR4 kinase domain.

Compound solubility studying

The solubility of each of the test compounds in PBS was measured by nephelometry using a NEPHELOstar plus apparatus (BMG Lab Technologies). This detection gave the amount of the particles in suspension by measuring the light that is diffused by the particles.

Liver microsomes stability evaluation

Microsomal incubations were carried out in 96-well plates. Briefly, reaction mixtures were created that contained mouse liver microsomes (0.33 mg/mL final protein concentration), 5 mM $MgCl_2$, 0.1 μM test compound, 1 mM NADPH and 0.1 M Tris/HCl buffer, pH 7.4. The test compounds were dissolved in dimethyl sulfoxide (DMSO) and diluted with 0.01% bovine serum albumin (BSA), and the final DMSO concentration used in the assay was 0.01% (v/v). Reactions were commenced with the addition of NADPH after pre-warming at 37°C for 10 min. Following incubation, an aliquot of 50 μL of the incubation sample was removed at 0, 7, 17, 30 and 60 min, and quenched with the same volume of methanol. The mixture was vortexed and centrifuged. Then the supernatant was subjected to LC-MS/MS analysis. All samples were prepared and analyzed in duplicates. Finally, the first-order rate of consumption of the compound (-k) and the *in vitro* $T_{1/2}$ values ($T_{1/2}$ = -0.693/k) were measured.[70, 71]

GSH binding affinity assay

The test compound (500 nM) was incubated with 2 mM GSH in methanol/PBS (15/85, v/v) solution at 37 °C. Aliquots were sampled at 0, 0.5, 1.0, 1.5, 2.1 and 19 h of incubation, and the reaction was stopped by the addition of 20 mM N-ethylmaleimide solution. The samples were determined by LC-MS/MS.

Blood stability evaluation

The test compound (5 μM) was incubated with fresh rat blood at 37 °C. Aliquots were sampled at 0, 0.5, 1.0, 2.0 and 5.0 h of incubation, and the reaction was stopped by protein precipitation in methanol. Then, the percentage of residual compound was determined by LC-MS/MS

***In Vivo* Pharmacokinetics (PK)**

The pharmacokinetic profiles were determined in SD rats, and the experiments were approved by the Bioethics Committee of the Shanghai Institute of Materia Medica, Chinese Academy of Sciences (IACUC: 2018-03-TW-05). Compound **15** (5% DMSO + 5% Tween-80 in 90% saline) was subjected to PK studies in SD rats. The test compound was administered via IV at 10 mg/kg, PO at 20 mg/kg and IP at 20mg/kg. After administration, blood samples were collected. The blood samples were centrifuged to obtain the plasma fraction. The plasma samples were deproteinized with methanol containing an internal standard. After centrifugation, the supernatant was diluted with methanol and centrifuged again. The compound concentrations of target compound in the supernatant was measured by LC/MS/MS.

Species difference study

Liver microsomal incubations were conducted in a total volume of 200 μL (liver microsomal incubation of human was 100 μL) containing human, mouse, rat, dog, and monkey liver microsomes (1.0×106 cells/mL), William's medium E formulation (pH 7.4), and substrate (3.0 μM). The corresponding mixture was preincubated in a water bath at 37 °C. After 180 min, the reaction was terminated by adding an equal volume of ice-cold acetonitrile, and stored at -70 °C until later analysis. All experiments were conducted in duplicate. For qualitative analysis, duplicate samples of each species were pooled. The combined samples were vortex-mixed and centrifuged at 14 000 rpm for 5 min. The supernatants were transferred into a glass tube, concentrated to dryness under a stream of nitrogen at 40 °C, and then reconstituted in 120 μL of acetonitrile with water (10: 90, v/v). After centrifugation at 14 000 rpm for 5 min, a 7-μL aliquot of each reconstituted solutions was analyzed by UPLC-UV/Q-TOF MS. Then, data were collected and processed by the software Analyst TF V1.6 (AB SCIEX, Framingham, MA, USA) and Masslynx V4.1 (Waters Corp., Milford, MA, USA) and analyzed with PeakView V1.2 and MetabolitePilot V1.5 from AB SCIEX.

ASSOCIATED CONTENT

Supporting Information. The structure, scores and FGFR1 inhibitory activities of the 112 compounds selected from the virtual screening; the inhibitory activities were determined by ELISA. X-ray crystal structure analysis: Data collection and refinement statistics. The Sequences coverage of the FGFR4 kinase domain by protein HPLC–MS/MS analysis. Residue Cys477 in FGFR4 was covalently modified by compound **10**. The inhibition ratios of kinases treated with 0.01 μM, 0.1 μM and 1 μM compound **15**, respectively. The UPLC-UV/Q-TOF MS analysis results of the metabolites of compound **15** in five different species liver cells from five different species, namely, human, monkey, dog, rat and mouse. The putative metabolic pathway of compound **15** in liver cells. HPLC analysis data of all the tested compounds.

Molecular formula strings (CSV).

Accession Codes

PDB codes are 6ITJ (FGFR1/**9**), 6IUP (FGFR4/**10**), and 6IUO (FGFR4/**11**). The authors will release the atomic coordinates and experimental data upon article publication.

AUTHOR INFORMATION

Corresponding Authors

*Phone: +86-21-50807042. E-mail: hliu@simm.ac.cn (Hong Liu)

*Phone: +86-21-50806600-2413. E-mail: jai@simm.ac.cn (Jing Ai)

*Phone: +86-21-50806600-1308. E-mail: myzheng@simm.ac.cn (Mingyue Zheng).

Author Contributions

†Y.W., Y.D. and X.W. contributed equally to this work.

Notes

The authors declare no competing financial interest.

ACKNOWLEDGEMENT

We gratefully acknowledge financial support from the National Natural Science Foundation of China (81773634 to M.Z., 81773762 to J.A, 81620108027 and 21632008 to H.L.), National Science & Technology Major Project "Key New Drug Creation and Manufacturing Program", China (2018ZX09711002), the Major Project of Chinese National Programs for Fundamental Research and Development (2015CB910304 to H.L.), "Personalized Medicines—Molecular Signature-based Drug Discovery and Development", Strategic Priority Research Pro-gram of the Chinese Academy of Sciences (XDA12050201 to M.Z. and XDA12050401 To H.J.).

ABBREVIATIONS USED

FGFRs, fibroblast growth factor receptors; FGFR, fibroblast growth factor receptor; RTKs, receptor tyrosine kinases; TKIs, tyrosine kinase inhibitors; VEGFRs, vascular endothelial growth receptors; PDGFRs, platelet-derived growth factor receptors; MOA, mechanism of action; CCA, cholangiocarcinoma; CADD, computer-aided drug design; PK, pharmacokinetics; VS, virtual screening; R^2, the square of Pearson Correlation Coefficient; SOM, site-of-metabolism; GSH, glutathione.

REFERENCES

(1) Tiong, K. H.; Mah, L. Y.; Leong, C. O. Functional roles of fibroblast growth factor receptors (FGFRs) signaling in human cancers. *Apoptosis* **2013,** 18, 1447-1468.

(2) Thisse, B.; Thisse, C. Functions and regulations of fibroblast growth factor signaling during embryonic development. *Dev. Biol.* **2005,** 287, 390-402.
(3) Dienstmann, R.; Rodon, J.; Prat, A.; Perez-Garcia, J.; Adamo, B.; Felip, E.; Cortes, J.; Iafrate, A. J.; Nuciforo, P.; Tabernero, J. Genomic aberrations in the FGFR pathway: opportunities for targeted therapies in solid tumors. *Ann. Oncol.* **2014,** 25, 552-563.
(4) Porta, R.; Borea, R.; Coelho, A.; Khan, S.; Araujo, A.; Reclusa, P.; Franchina, T.; Van Der Steen, N.; Van Dam, P.; Ferri, J.; Sirera, R.; Naing, A.; Hong, D.; Rolfo, C. FGFR a promising druggable target in cancer: molecular biology and new drugs. *Crit. Rev. Oncol. Hematol.* **2017,** 113, 256-267.
(5) Babina, I. S.; Turner, N. C. Advances and challenges in targeting FGFR signalling in cancer. *Nat. Rev. Cancer* **2017,** 17, 318-332.
(6) Izzedine, H.; Ederhy, S.; Goldwasser, F.; Soria, J. C.; Milano, G.; Cohen, A.; Khayat, D.; Spano, J. P. Management of hypertension in angiogenesis inhibitor-treated patients. *Ann. Oncol.* **2009**, 20, 807-815.
(7) Ricciardi, S.; Tomao, S.; de Marinis, F. Toxicity of targeted therapy in non-small-cell lung cancer management. *Clin. Lung Cancer* **2009**, 10, 28-35.
(8) Katoh, M. Fibroblast growth factor receptors as treatment targets in clinical oncology. *Nat. Rev. Clin. Oncol.* **2019**, 16, 105-122.
(9) Gavine, P. R.; Mooney, L.; Kilgour, E.; Thomas, A. P.; Al-Kadhimi, K.; Beck, S.; Rooney, C.; Coleman, T.; Baker, D.; Mellor, M. J.; Brooks, A. N.; Klinowska, T. AZD4547: an orally bioavailable, potent, and selective inhibitor of the fibroblast growth factor receptor tyrosine kinase family. *Cancer Res.* **2012,** 72, 2045-2056.
(10) Guagnano, V.; Furet, P.; Spanka, C.; Bordas, V.; Le Douget, M.; Stamm, C.; Brueggen, J.; Jensen, M. R.; Schnell, C.; Schmid, H.; Wartmann, M.; Berghausen, J.; Drueckes, P.; Zimmerlin, A.; Bussiere, D.; Murray, J.; Graus Porta, D. Discovery of 3-(2,6-dichloro-3,5-dimethoxy-phenyl)-1--1-methyl-urea (NVP-BGJ398), a potent and selective inhibitor of the fibroblast growth factor receptor family of receptor tyrosine kinase. *J. Med. Chem.* **2011,** 54, 7066-7083.
(11) Watanabe Miyano, S.; Yamamoto, Y.; Kodama, K.; Miyajima, Y.; Mikamoto, M.; Nakagawa, T.; Kuramochi, H.; Funasaka, S.; Nagao, S.; Sugi, N. H.; Okamoto, K.; Minoshima, Y.; Nakatani, Y.; Karoji, Y.; Ohashi, I.; Yamane, Y.; Okada, T.; Matsushima, T.; Matsui, J.; Iwata, M.; Uenaka, T.; Tsuruoka, A. E7090, a novel selective inhibitor of fibroblast growth factor receptors, displays potent antitumor activity and prolongs survival in preclinical models. *Mol. Cancer Ther.* **2016,** 15, 2630-2639.
(12) Zhao, G.; Li, W. Y.; Chen, D.; Henry, J. R.; Li, H. Y.; Chen, Z.; Zia-Ebrahimi, M.; Bloem, L.; Zhai, Y.; Huss, K.; Peng, S. B.; McCann, D. J. A novel, selective inhibitor of fibroblast growth factor receptors that shows a potent broad spectrum of antitumor activity in several tumor xenograft models. *Mol. Cancer Ther.* **2011,** 10, 2200-2210.
(13) Perera, T. P. S.; Jovcheva, E.; Mevellec, L.; Vialard, J.; De Lange, D.; Verhulst, T.; Paulussen, C.; Van De Ven, K.; King, P.; Freyne, E.; Rees, D. C.; Squires, M.; Saxty, G.; Page, M.; Murray, C. W.; Gilissen, R.; Ward, G.; Thompson, N. T.; Newell, D. R.; Cheng, N.; Xie, L.; Yang, J.; Platero, S. J.; Karkera, J. D.; Moy, C.; Angibaud, P.; Laquerre, S.; Lorenzi, M. V. Discovery and pharmacological characterization of JNJ-42756493 (Erdafitinib), a functionally selective small-molecule FGFR family inhibitor. *Mol. Cancer Ther.* **2017,** 16, 1010-1020.
(14) Nakanishi, Y.; Akiyama, N.; Tsukaguchi, T.; Fujii, T.; Sakata, K.; Sase, H.; Isobe, T.; Morikami, K.; Shindoh, H.; Mio, T.; Ebiike, H.; Taka, N.; Aoki, Y.; Ishii, N. The fibroblast growth factor receptor genetic status as a potential predictor of the sensitivity to

CH5183284/Debio 1347, a novel selective FGFR inhibitor. *Mol. Cancer Ther.* **2014,** 13, 2547-2558.
(15) Goyal, L.; Arkenau, H.-T.; Tran, B.; Soria, J.-C.; Bahleda, R.; Mak, G.; Zhu, A.; Javle, M.; Hiroshi, H.; Benedetti, F.; Huang, J.; Winkler, R.; Meric-Bernstam, F. Early clinical efficacy of TAS-120, a covalently bound FGFR inhibitor, in patients with cholangiocarcinoma. *Ann. Oncol.* **2017,** 28, I45-I45.
(16) Meric-Bernstam, F.; Arkenau, H.; Tran, B.; Bahleda, R.; Kelley, R.; Hierro, C.; Ahn, D.; Zhu, A.; Javle, M.; Winkler, R.; He, H.; Huang, J.; Goyal, L. Efficacy of TAS-120, an irreversible Fibroblast Growth Factor Receptor (FGFR) inhibitor, in cholangiocarcinoma patients with FGFR pathway alterations who were previously treated with chemotherapy and other FGFR inhibitors. *Ann. Oncol.* **2018,** 29, 1-1.
(17) Paik, P. K.; Shen, R.; Berger, M. F.; Ferry, D.; Soria, J. C.; Mathewson, A.; Rooney, C.; Smith, N. R.; Cullberg, M.; Kilgour, E.; Landers, D.; Frewer, P.; Brooks, N.; Andre, F. A Phase Ib open-label multicenter study of AZD4547 in patients with advanced squamous cell lung cancers. *Clin. Cancer Res.* **2017,** 23, 5366-5373.
(18) Seckl, M.; Badman, P. D.; Liu, X.; MacPherson, I. R.; Zubairi, I. H.; Baird, R. D.; Garcia-Corbacho, J.; Cresti, N.; Plummer, E. R.; Armstrong, A. C.; Allerton, R.; Landers, D.; Nicholas, H.; McLellan, L.; Lim, A. K.; Coombes, C. RADICAL trial: a phase Ib/IIa study to assess the safety and efficacy of AZD4547 in combination with either anastrozole or letrozole in ER positive breast cancer patients progressing on these aromatase inhibitors (AIs). *J. Clin. Oncol.* **2017,** 35, 1059-1059.
(19) Goyal, L.; Liu, L. Y.; Lennerz, J. K.; Harding, J. J.; Huang, J.; Winkler, R.; Hiroshi, H.; Ting, D. T.; Juric, D.; Corcoran, R. B.; El-Bardeesy, N.; Zhu, A. X. Abstract LB-092: TAS120, a covalently-binding FGFR inhibitor (FGFRi), overcomes resistance to BGJ398 in patients with FGFR2 fusion positive cholangiocarcinoma. *Cancer Res.* **2018,** 78, LB-092-LB-092.
(20) Wang, Y.; Li, L.; Zhang, B.; Xing, J.; Chen, S.; Wan, W.; Song, Y.; Jiang, H.; Jiang, H.; Luo, C.; Zheng, M. Discovery of novel disruptor of silencing telomeric 1-like (DOT1L) inhibitors using a target-specific scoring function for the (S)-Adenosyl-l-methionine (SAM)-dependent methyltransferase family. *J. Med. Chem.* **2017,** 60, 2026-2036.
(21) Chen, H.; Ma, J.; Li, W.; Eliseenkova, A. V.; Xu, C.; Neubert, T. A.; Miller, W. T.; Mohammadi, M. A molecular brake in the kinase hinge region regulates the activity of receptor tyrosine kinases. *Mol. Cell* **2007,** 27, 717-730.
(22) Huang, Z.; Chen, H.; Blais, S.; Neubert, T. A.; Li, X.; Mohammadi, M. Structural mimicry of a-loop tyrosine phosphorylation by a pathogenic FGF receptor 3 mutation. *Structure* **2013,** 21, 1889-1896.
(23) Liu, T.; Lin, Y.; Wen, X.; Jorissen, R. N.; Gilson, M. K. BindingDB: a web-accessible database of experimentally determined protein-ligand binding affinities. *Nucleic Acids Res.* **2007,** 35, D198-201.
(24) Friesner, R. A.; Banks, J. L.; Murphy, R. B.; Halgren, T. A.; Klicic, J. J.; Mainz, D. T.; Repasky, M. P.; Knoll, E. H.; Shelley, M.; Perry, J. K.; Shaw, D. E.; Francis, P.; Shenkin, P. S. Glide: a new approach for rapid, accurate docking and scoring. 1. Method and assessment of docking accuracy. *J. Med. Chem.* **2004,** 47, 1739-1749.
(25) Shen, Q.; Xiong, B.; Zheng, M.; Luo, X.; Luo, C.; Liu, X.; Du, Y.; Li, J.; Zhu, W.; Shen, J.; Jiang, H. Knowledge-based scoring functions in drug design: 2. can the knowledge base be enriched? *J. Chem. Inf. Model.* **2011,** 51, 386-397.

(26) Chih-Chung, C.; Chih-Jen, L. Chang, C. C.; Lin, C. J. LIBSVM: a library for support vector machines. *ACM Trans. Intell. Syst. Technol.* **2011**, 2, 1−39..
(27) Guyon, I.; Weston, J.; Barnhill, S.; Vapnik, V. Gene selection for cancer classification using support vector machines. *Machine Learning* **2002,** 46, 389-422.
(28) Baell, J. B.; Holloway, G. A. New substructure filters for removal of pan assay interference compounds (PAINS) from screening libraries and for their exclusion in bioassays. *J. Med. Chem.* **2010,** 53, 2719-2740.
(29) Rogers, D.; Hahn, M. Extended-connectivity fingerprints. *J. Chem. Inf. Model.* **2010,** 50, 742-754.
(30) Zhang, J.; Yang, P. L.; Gray, N. S. Targeting cancer with small molecule kinase inhibitors. *Nat. Rev. Cancer* **2009**, 9, 28-39.
(31) Zhao, Z.; Bourne, P. E. Progress with covalent small-molecule kinase inhibitors. *Drug Discov. Today* **2018**, 23, 727-735.
(32) Roskoski, R., Jr. Properties of FDA-approved small molecule protein kinase inhibitors. *Pharmacol. Res.* **2019**, 144, 19-50.
(33) Liu, Q.; Sabnis, Y.; Zhao, Z.; Zhang, T.; Buhrlage, S. J.; Jones, L. H.; Gray, N. S. Developing irreversible inhibitors of the protein kinase cysteinome. *Chem. Biol.* **2013**, 20, 146-59.
(34) Zhao, Z.; Liu, Q.; Bliven, S.; Xie, L.; Bourne, P. E. Determining cysteines available for covalent inhibition across the human kinome. *J. Med. Chem.* **2017**, 60, 2879-2889.
(35) Zhou, W.; Hur, W.; McDermott, U.; Dutt, A.; Xian, W.; Ficarro, S. B.; Zhang, J.; Sharma, S. V.; Brugge, J.; Meyerson, M.; Settleman, J.; Gray, N. S. A structure-guided approach to creating covalent FGFR inhibitors. *Chem. Biol.* **2010,** 17, 285-295.
(36) Zheng, M.; Luo, X.; Shen, Q.; Wang, Y.; Du, Y.; Zhu, W.; Jiang, H. Site of metabolism prediction for six biotransformations mediated by cytochromes P450. *Bioinformatics* **2009,** 25, 1251-1258.
(37) Peng, J.; Lu, J.; Shen, Q.; Zheng, M.; Luo, X.; Zhu, W.; Jiang, H.; Chen, K. *In silico* site of metabolism prediction for human UGT-catalyzed reactions. *Bioinformatics* **2014,** 30, 398-405.
(38) Rydberg, P.; Gloriam, D. E.; Zaretzki, J.; Breneman, C.; Olsen, L. SMARTCyp: A 2D method for prediction of Cytochrome P450-mediated drug metabolism. *ACS Med. Chem. Lett.* **2010,** 1, 96-100.
(39) Li, J.; Schneebeli, S. T.; Bylund, J.; Farid, R.; Friesner, R. A. IDSite: an accurate approach to predict P450-mediated drug metabolism. *J. Chem. Theory Comput.* **2011,** 7, 3829-3845.
(40) Baillie, T. A. Targeted covalent inhibitors for drug design. *Angew. Chem. Int. Ed.* **2016,** 55, 13408-13421.
(41) Singh, J.; Petter, R. C.; Baillie, T. A.; Whitty, A. The resurgence of covalent drugs. *Nat. Rev. Drug Discov.* **2011,** 10, 307-317.
(42) Mah, R.; Thomas, J. R.; Shafer, C. M. Drug discovery considerations in the development of covalent inhibitors. *Bioorg. Med. Chem. Lett.* **2014,** 24, 33-39.
(43) De Cesco, S.; Kurian, J.; Dufresne, C.; Mittermaier, A. K.; Moitessier, N. Covalent inhibitors design and discovery. *Eur. J. Med. Chem.* **2017,** 138, 96-114.
(44) Tsou, H. R.; Mamuya, N.; Johnson, B. D.; Reich, M. F.; Gruber, B. C.; Ye, F.; Nilakantan, R.; Shen, R.; Discafani, C.; DeBlanc, R.; Davis, R.; Koehn, F. E.; Greenberger, L. M.; Wang, Y. F.; Wissner, A. 6-Substituted-4-(3-bromophenylamino)quinazolines as putative irreversible inhibitors of the epidermal growth factor receptor (EGFR) and human epidermal growth factor

receptor (HER-2) tyrosine kinases with enhanced antitumor activity. *J. Med. Chem.* **2001,** 44, 2719-2734.
(45) Byrd, J. C.; Furman, R. R.; Coutre, S. E.; Flinn, I. W.; Burger, J. A.; Blum, K. A.; Grant, B.; Sharman, J. P.; Coleman, M.; Wierda, W. G.; Jones, J. A.; Zhao, W.; Heerema, N. A.; Johnson, A. J.; Sukbuntherng, J.; Chang, B. Y.; Clow, F.; Hedrick, E.; Buggy, J. J.; James, D. F.; O'Brien, S. Targeting BTK with ibrutinib in relapsed chronic lymphocytic leukemia. *N. Engl. J. Med.* **2013,** 369, 32-42.
(46) FDA Imbruvica review. *U.S. Food&Drug Administration* **2013**.
(47) Dungo, R. T.; Keating, G. M. Afatinib: first global approval. *Drugs* **2013,** 73, 1503-1515.
(48) Leung, L.; Yang, X.; Strelevitz, T. J.; Montgomery, J.; Brown, M. F.; Zientek, M. A.; Banfield, C.; Gilbert, A. M.; Thorarensen, A.; Dowty, M. E. Clearance prediction of targeted covalent inhibitors by *in vitro-in vivo* extrapolation of hepatic and extrahepatic clearance mechanisms. *Drug Metab. Dispos.* **2017,** 45, 1-7.
(49) Moghaddam, M. F.; Tang, Y.; O'Brien, Z.; Richardson, S. J.; Bacolod, M.; Chaturedi, P.; Apuy, J.; Kulkarni, A. A proposed screening paradigm for discovery of covalent inhibitor drugs. *Drug Metab. Lett.* **2014,** 8, 19-30.
(50) Strelow, J. M. A perspective on the kinetics of covalent and irreversible inhibition. *Slas. Discovery* **2017**, 22, 3-20.
(51) Brameld, K. A.; Owens, T. D.; Verner, E.; Venetsanakos, E.; Bradshaw, J. M.; Phan, V. T.; Tam, D.; Leung, K.; Shu, J.; LaStant, J.; Loughhead, D. G.; Ton, T.; Karr, D. E.; Gerritsen, M. E.; Goldstein, D. M.; Funk, J. O. Discovery of the irreversible covalent FGFR inhibitor 8-(3-(4-Acryloylpiperazin-1-yl)propyl)-6-(2,6-dichloro-3,5-dimethoxyphenyl)-2-(methylamino)pyrido[2,3-*d*]pyrimidin-7(8*H*)-one (PRN1371) for the Treatment of Solid Tumors. *J. Med. Chem.* **2017**, 60, 6516-6527.
(52) Schwartz, P. A.; Kuzmic, P.; Solowiej, J.; Bergqvist, S.; Bolanos, B.; Almaden, C.; Nagata, A.; Ryan, K.; Feng, J. L.; Dalvie, D.; Kath, J. C.; Xu, M. R.; Wani, R.; Murray, B. W. Covalent EGFR inhibitor analysis reveals importance of reversible interactions to potency and mechanisms of drug resistance. *Proc. Natl. Acad. Sci. U.S.A* **2014**, 111, 173-178.
(53) Eid, S.; Turk, S.; Volkamer, A.; Rippmann, F.; Fulle, S. KinMap: a web-based tool for interactive navigation through human kinome data. *BMC Bioinformatics* **2017,** 18, 16, 1-6.
(54) Mohammad, S.; Zhou, Z.; Gong, Q.; January, C. T. Blockage of the hERG human cardiac K^+ channel by the gastrointestinal prokinetic agent cisapride. *Am. J. Physiol.* **1997,** 273, H2534-H2538.
(55) Pollard, C. E.; Skinner, M.; Lazic, S. E.; Prior, H. M.; Conlon, K. M.; Valentin, J. P.; Dota, C. An analysis of the relationship between preclinical and clinical QT interval-related data. *Toxicol. Sci.* **2017,** 159, 94-101.
(56) Yao, X.; Anderson, D. L.; Ross, S. A.; Lang, D. G.; Desai, B. Z.; Cooper, D. C.; Wheelan, P.; McIntyre, M. S.; Bergquist, M. L.; MacKenzie, K. I.; Becherer, J. D.; Hashim, M. A. Predicting QT prolongation in humans during early drug development using hERG inhibition and an anaesthetized guinea-pig model. *Br. J. Pharmacol.* **2008,** 154, 1446-1456.
(57) Ban, F.; Dalal, K.; Li, H.; LeBlanc, E.; Rennie, P. S.; Cherkasov, A. Best practices of computer-aided drug discovery: lessons learned from the development of a preclinical candidate for prostate cancer with a new mechanism of action. *J. Chem. Inf. Model* **2017,** 57, 1018-1028.
(58) Manglik, A.; Lin, H.; Aryal, D. K.; McCorvy, J. D.; Dengler, D.; Corder, G.; Levit, A.; Kling, R. C.; Bernat, V.; Hubner, H.; Huang, X. P.; Sassano, M. F.; Giguere, P. M.; Lober, S.;

Da, D.; Scherrer, G.; Kobilka, B. K.; Gmeiner, P.; Roth, B. L.; Shoichet, B. K. Structure-based discovery of opioid analgesics with reduced side effects. *Nature* **2016,** 537, 185-190.
(59) Warren, G. L.; Andrews, C. W.; Capelli, A. M.; Clarke, B.; LaLonde, J.; Lambert, M. H.; Lindvall, M.; Nevins, N.; Semus, S. F.; Senger, S.; Tedesco, G.; Wall, I. D.; Woolven, J. M.; Peishoff, C. E.; Head, M. S. A critical assessment of docking programs and scoring functions. *J. Med. Chem.* **2006,** 49, 5912-5931.
(60) Zhu, K.; Borrelli, K. W.; Greenwood, J. R.; Day, T.; Abel, R.; Farid, R. S.; Harder, E. Docking covalent inhibitors: a parameter free approach to pose prediction and scoring. *J. Chem. Inf. Model* **2014,** 54, 1932-1940.
(61) Tsou, H. R.; Overbeek-Klumpers, E. G.; Hallett, W. A.; Reich, M. F.; Floyd, M. B.; Johnson, B. D.; Michalak, R. S.; Nilakantan, R.; Discafani, C.; Golas, J.; Rabindran, S. K.; Shen, R.; Shi, X.; Wang, Y. F.; Upeslacis, J.; Wissner, A. Optimization of 6,7-disubstituted-4-(arylamino)quinoline-3-carbonitriles as orally active, irreversible inhibitors of human epidermal growth factor receptor-2 kinase activity. *J. Med. Chem.* **2005**, 48, 1107-1131.
(62) Jiang, A.; Liu, Q.; Wang, R.; Wei, P.; Dai, Y.; Wang, X.; Xu, Y.; Ma, Y.; Ai, J.; Shen, J.; Ding, J.; Xiong, B. Structure-based discovery of a series of 5H-Pyrrolo[2,3-b]pyrazine FGFR kinase inhibitors. *Molecules* **2018,** 23, 1-19.
(63) Seeliger, M. A.; Young, M.; Henderson, M. N.; Pellicena, P.; King, D. S.; Falick, A. M.; Kuriyan, J. High yield bacterial expression of active c-Abl and c-Src tyrosine kinases. *Protein Sci.* **2005,** 14, 3135-3139.
(64) Kabsch, W. XDS. *Acta Crystallogr. D Biol. Crystallogr.* **2010,** 66, 125-132.
(65) Minor, W.; Cymborowski, M.; Otwinowski, Z.; Chruszcz, M. HKL-3000: the integration of data reduction and structure solution--from diffraction images to an initial model in minutes. *Acta Crystallogr. D Biol. Crystallogr.* **2006,** 62, 859-866.
(66) McCoy, A. J.; Grosse-Kunstleve, R. W.; Adams, P. D.; Winn, M. D.; Storoni, L. C.; Read, R. J. Phaser crystallographic software. *J. Appl. Crystallogr.* **2007,** 40, 658-674.
(67) Huang, Z.; Tan, L.; Wang, H.; Liu, Y.; Blais, S.; Deng, J.; Neubert, T. A.; Gray, N. S.; Li, X.; Mohammadi, M. DFG-out mode of inhibition by an irreversible type-1 inhibitor capable of overcoming gate-keeper mutations in FGF receptors. *ACS Chem. Biol.* **2015,** 10, 299-309.
(68) Adams, P. D.; Afonine, P. V.; Bunkoczi, G.; Chen, V. B.; Davis, I. W.; Echols, N.; Headd, J. J.; Hung, L.-W.; Kapral, G. J.; Grosse-Kunstleve, R. W.; McCoy, A. J.; Moriarty, N. W.; Oeffner, R.; Read, R. J.; Richardson, D. C.; Richardson, J. S.; Terwilliger, T. C.; Zwart, P. H. PHENIX: a comprehensive Python-based system for macromolecular structure solution. *Acta Crystallogr. D Biol. Crystallogr.* **2010,** 66, 213-221.
(69) Emsley, P.; Lohkamp, B.; Scott, W. G.; Cowtan, K. Features and development of Coot. *Acta Crystallogr. D Biol. Crystallogr.* **2010,** 66, 486-501.
(70) Obach, R. S. Prediction of human clearance of twenty-nine drugs from hepatic microsomal intrinsic clearance data: an examination of *in vitro* half-life approach and nonspecific binding to microsomes. *Drug Metab. Dispos.* **1999**, 27, 1350-1359.
(71) Nikolic, K.; Agababa, D. Prediction of hepatic microsomal intrinsic clearance and human clearance values for drugs. *J. Mol. Graph. Model.* **2009**, 28, 245-252.

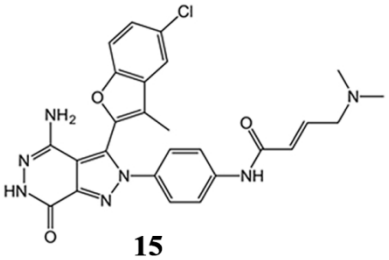

15

FGFR1 IC_{50}: 20.4±0.9 nM

FGFR IC_{50}: 7.2±3.6 nM

KG1 cell IC_{50}: 3.7±2.5 nM

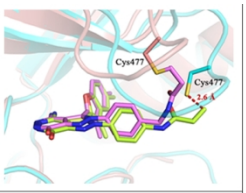

K_i: 10 nM

K_{inact}/K_i: 0.07 $\mu M^{-1}s^{-1}$

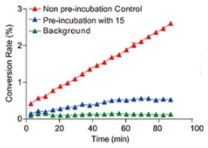

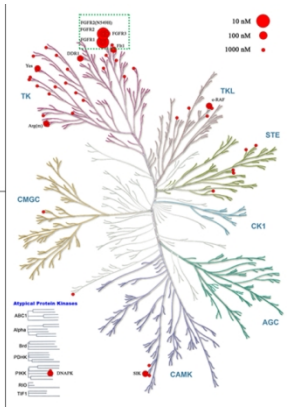

Table of contents

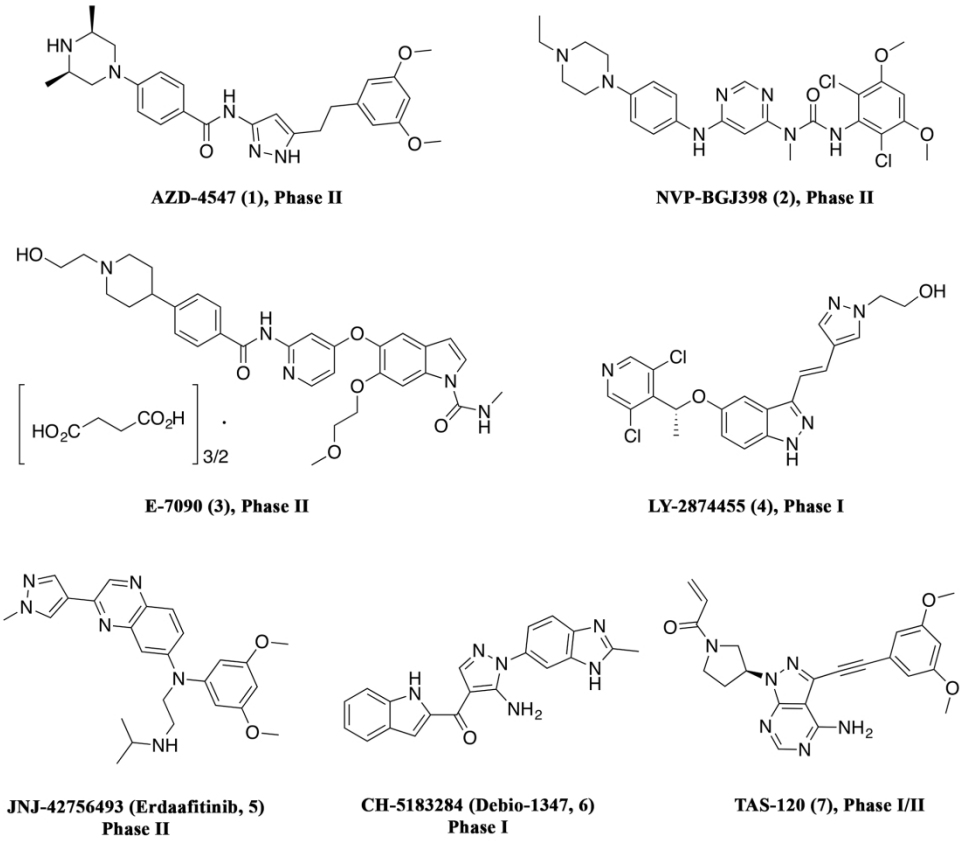

Figure 1. FGFR-selective inhibitors in clinical development.

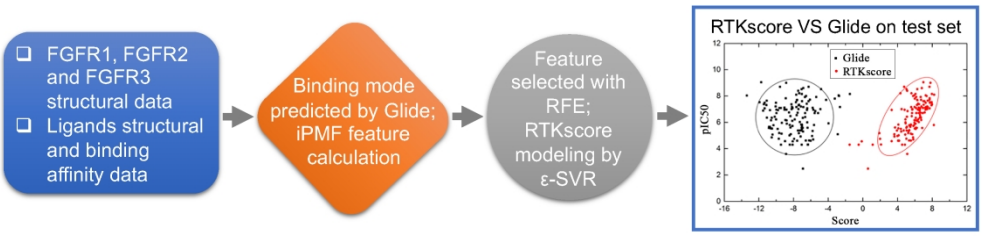

Figure 2. Workflow of RTKscore development and comparation of RTKscore with Glide on a test set.

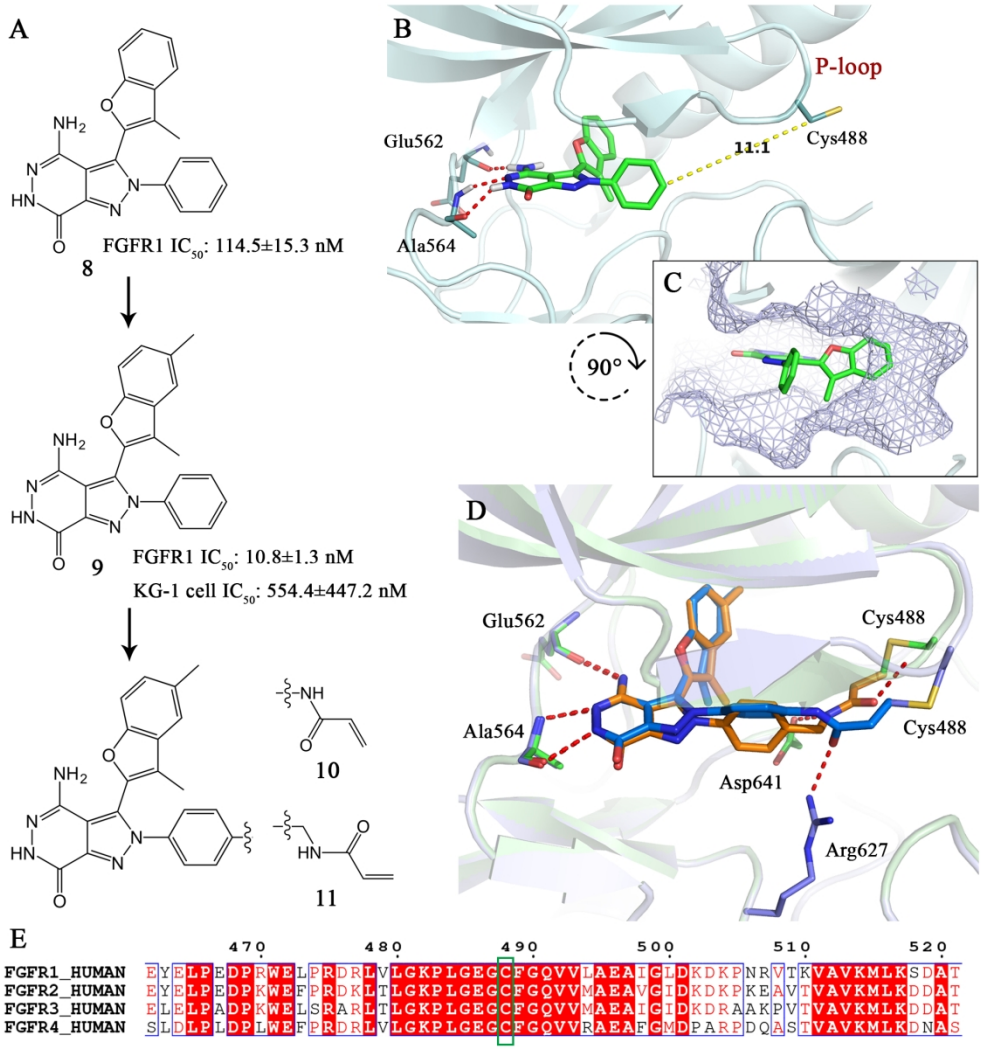

Figure 3. (A) The structures of compounds **8**, **9**, **10** and **11**; (B) putative binding mode of compound **8** with FGFR1(PDB code: 3TT0); (C) the active site pocket of FGFR1 depicted as mesh surface. (D) the putative binding modes of compound **10** (blue) and compound **11** (orange) with FGFR1 simulated by covalent docking. (E) FGFR1, FGFR2, FGFR3 and FGFR4 P-loop sequence alignment.

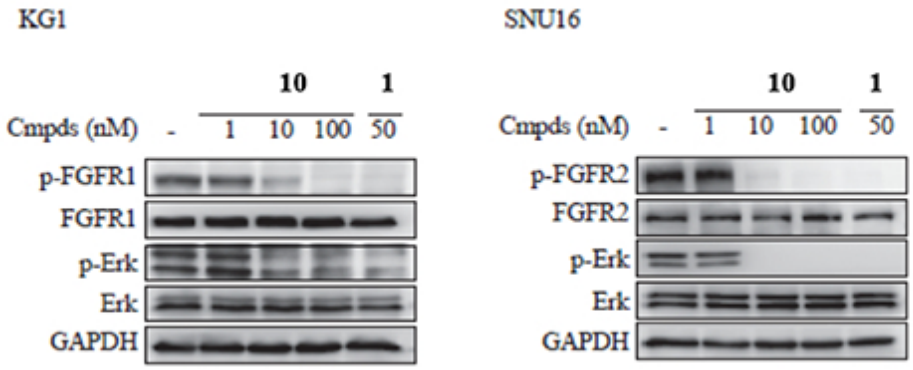

Figure 4. The effects of compound **10** on the phosphorylation of FGFR and the downstream effector Erk in the KG1 and SNU16 cell lines.

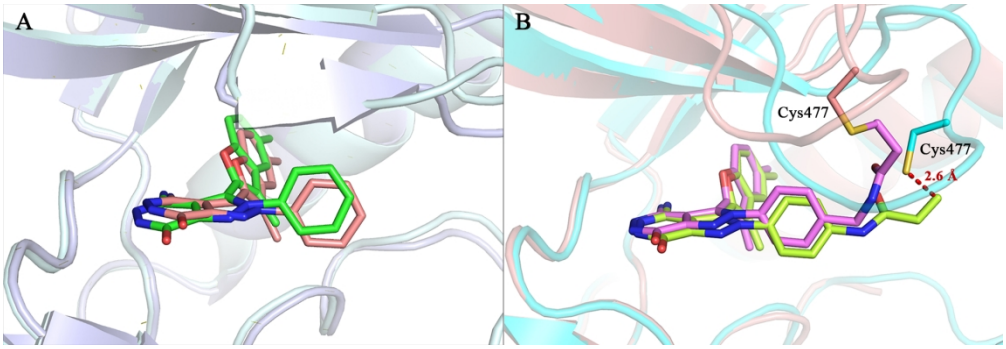

Figure 5. (A) The cocrystal structure (shown in green) of compound **9** and the FGFR1 complex (PDB id: 6ITJ) and the putative binding mode (shown in pink) of compound **9** and FGFR1 simulated by molecular docking. (B) The crystal structures of the complex of compound **10** (shown in magenta) with FGFR4 (shown in salmon) (PDB id: 6IUP) and the complex of compound **11** (shown in lemon) with FGFR4 (shown in cyan) (PDB id: 6IUO).

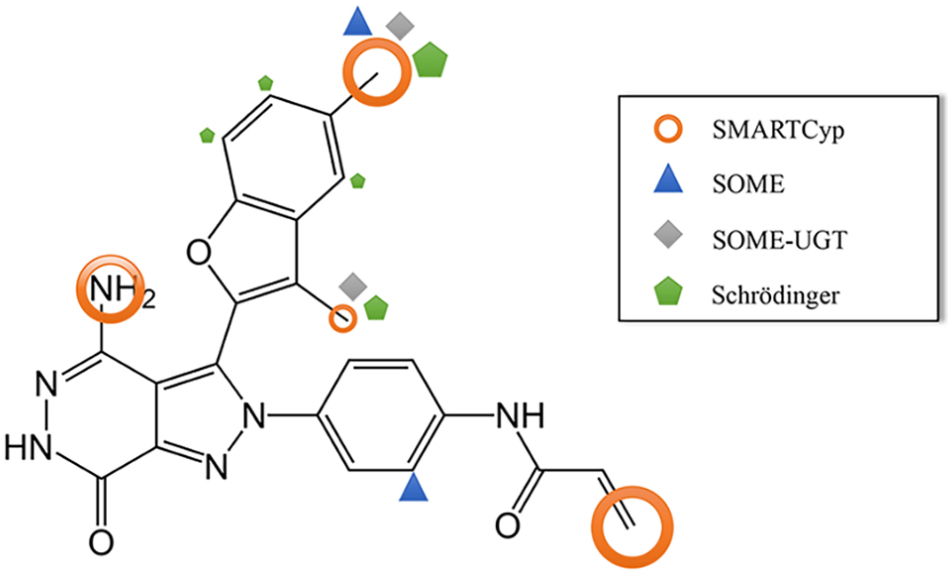

Figure 6. SOM prediction of compound **10** by three programs. SMARTCyp (orange circles, metabolism probability ordered by size of circle), SOME (blue triangles) and SOME-UGT (grey diamonds), and Schrödinger (green pentagons, metabolism probability ordered by size).

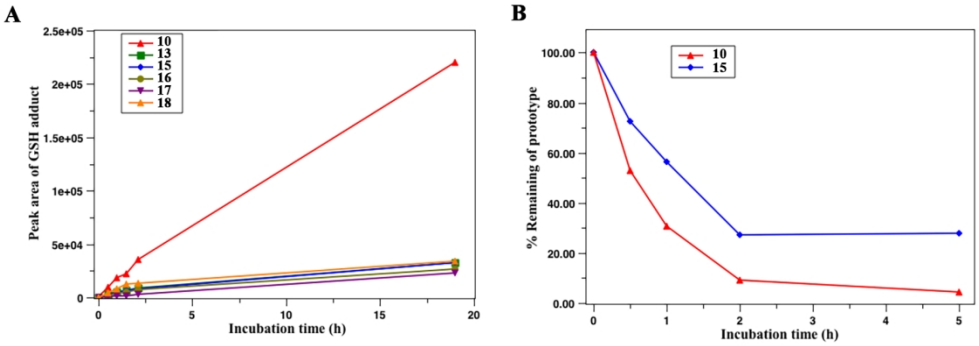

Figure 7. (A) GSH affinity evaluation of compounds **10**, **13**, **15**, and **16**; (B) blood stability evaluation of compounds **10** and **15**.

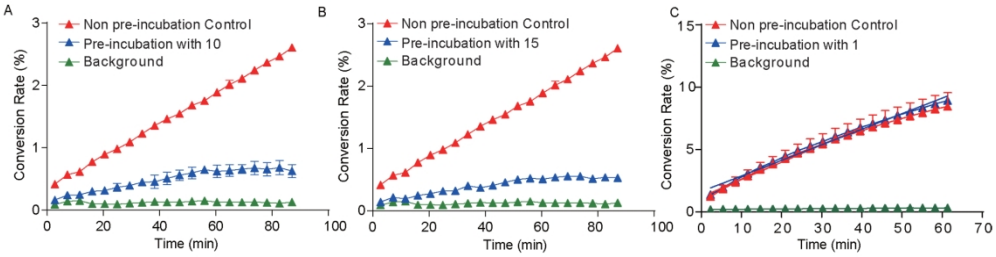

Figure 8. Compound **10** (A) and **15** (B) irreversibly binds to FGFR1. Enzyme activity of FGFR1 was assayed by a Caliper EZ Reader under three different conditions: without the enzyme (background), without the compound (non-pre-incubation control), and pre-incubated with the compound. "Conversion" here represents the enzyme activity and means "the percent of conversion of the substrate peptide".

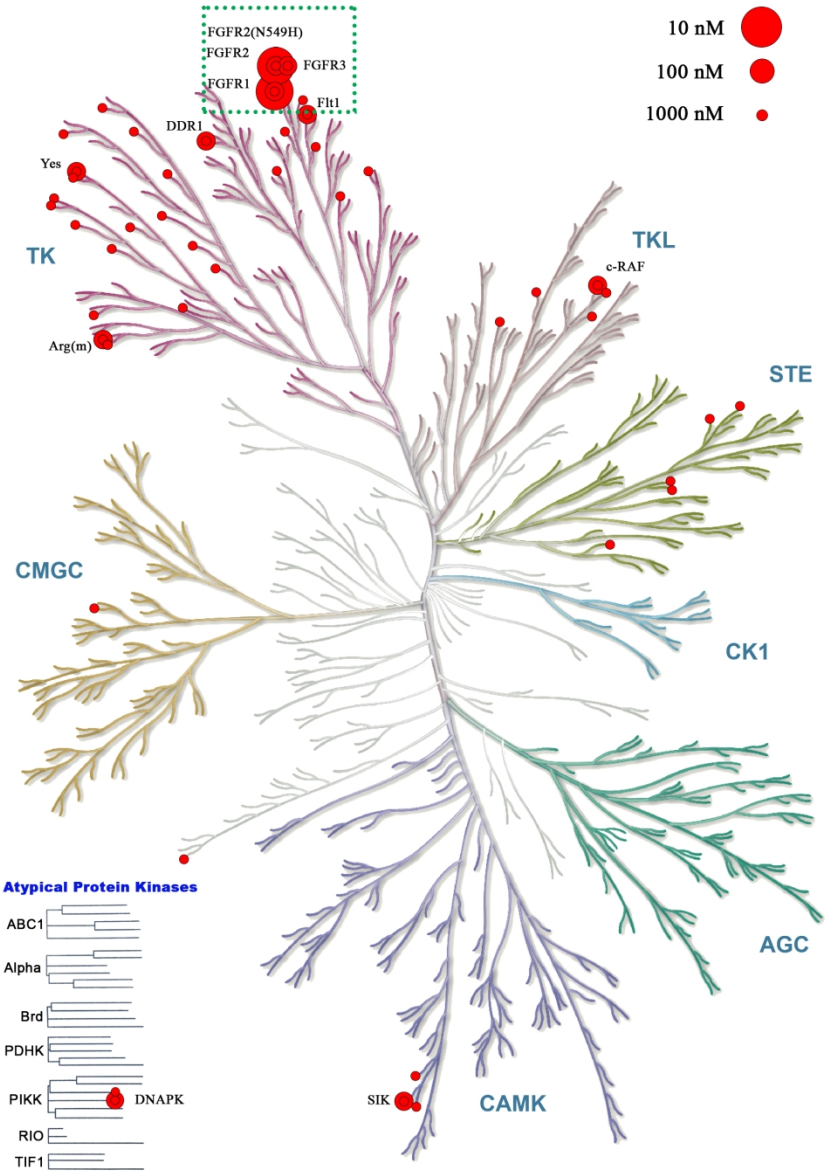

Figure 9. Kinase profile of compound **15** drawn with KinMap.[53] Kinase inhibition ratios above 50% at corresponding concentrations are marked as red circles.